Full Waveform Inversion
of shallow seismic Rayleigh waves to
characterize the "Ettlinger Linie"

Anwendung der Wellenforminversion von Rayleigh Wellen zur Bestimmung der "Ettlinger Linie"

Master's Thesis of

Marvin Binnig

at the Department of Physics
Geophysical Institute

Reviewer: Prof. Dr. Thomas Bohlen
Second reviewer: Prof. Dr. Friedemann Wenzel

26. October 2015

Fakultät für Physik
Karlsruher Institut für Technologie
76128 Karlsruhe

I declare that I have developed and written the enclosed thesis completely by myself, and have not used sources or means without declaration in the text.

Karlsruhe, 26.10.2015

. . . .

(Marvin Binnig)

Contents

1. Introduction

Shallow-seismic Rayleigh waves are attractive for geotechnical site investigations. They exhibit a high signal to noise ratio in field data recordings and reveal a high sensitivity to the S-wave velocity, an important lithological and geotechnical parameter to characterize the very shallow subsurface. Established inversion methods assume (local) 1-D subsurface models, and allow the reconstruction of the S-wave velocity as a function of depth by inverting the dispersion properties of the Rayleigh waves (e.g. Forbriger (2003a), Forbriger (2003b) Wathelet et al. (2004), Socco et al. (2010)). These classical methods, however, fail if significant lateral variations of medium properties are present. Then the full waveform inversion (FWI) of the elastic wave field is considered to obtain reasonable solutions. The method of FWI is rising in popularity as present day computers are capable of inverting the complete wave field in reasonable time, nevertheless, approaches to apply this method to surface waves, in particular Rayleigh waves, are still rare (e.g. Groos (2013) ,Schäfer (2014)).

In this thesis I present the results of two-dimensional viscoelastic full waveform inversion applied to field data sets recorded in an area, which exhibits severe lateral property variations, in order to proof the feasibility of FWI. The structure of the anomaly is determined thoroughly in previous works ((Stövhase, 2015), (Lüttschwager, 2014)) and allows consequently an instant verification of the obtained results. The utilized FWI code processes in time domain, using finite differences method to solve the elastic wave equation (Virieux, 1986), (Levander, 1988), (Bohlen, 2002). In order to enhance the quality of the data misfit a multi-scale approach as suggested by Bunks et al. (1995) is used, which enables step wise inversion of seismic signals with low frequency content to high frequency content. The study area reveals predominantly depth dependent subsurface characteristics crossed by a wedge-shaped structure with the extent of approximately 2 meters depth and 10 meters width, providing ideal conditions in terms of very shallow subsurface surveys realized with low effort. Data acquisition is performed orthogonal to the structure in order to allow for the simulation of two-dimensional wave propagation.

The thesis is divided into five topics, beginning with the characterization of the investigation site and proceeding to the substantial theoretical background, that is mandatory in order to understand the basics of Rayleigh wave inversion. Subsequently I present the raw field data and illustrate the very first data processing, such that it satisfies the requirements of the inversion algorithm. In the following chapter I go into detail of the complete routine of the applied full waveform inversion on the basis of the recorded field data set and, finally, present my results in terms of misfit reduction, seismogram fitting and estimated subsurface models including the parameters S-wave velocity, P-wave velocity and mass density.

2. Study Area

The application of two-dimensional full waveform inversion to field data demands certain properties from the recorded seismic wave field. It is desirable to obtain signals of the seismic wave field, which interferes exclusively with the subsurface in the plane of the aligned geophones. Reflections, for example, emerging from out of this plane would be interpreted as corresponding to material properties lying in that plane. In other words, the study area must exhibit a two-dimensional subsurface structure. Fortunately, the material properties of the investigation site are well analyzed in previous works (e.g. Zacharias (2010), Groos (2013), Schäfer (2014)), and seem to satisfy the requirements of a predominantly depth-dependent geological structure. Furthermore, my colleague Gunther Lüttschwager identifies a formation with significantly lower seismic velocities compared to the surrounding material, crossing this area (Lüttschwager, 2014). This anomaly seems to form a perfectly straight line over a distance of at least 50 meters with reasonable depth and width in terms of very shallow surface surveys. For the purpose of a detailed characterization of the anomaly Stövhase (2015) performs traveltime tomography of Love waves and evaluates a wedge shaped trench with the dimensions of approximately 2.5 meters depth and 10 meters width. A set-up of the acquisition geometry orthogonal to the low-velocity structure and, furthermore, assuming a penetration depth of Rayleigh waves easily exceeding the bottom of the trench, seems promising in the sense of a successful application of full waveform inversion. The site is located southwest of the city of Karlsruhe and is part of the gliding airfield of Rheinstetten (see figure 2.1).

2.1. Geological Setting and History

The near subsurface of the study area is covered by fluviatile sediments of the river Rhein consisting of gravel and sand, which was deposited in late pleistocene (Hüttner et al., 1986). The topmost layer of the subsurface is assumed to consist of dry or only partially saturated material due to the absence of rain at the time the measurements are performed. Groos (2013) estimates the groundwater table at the site to a depth of about 6.8 meter, whereas Zacharias (2010) evaluates a depth of the groundwater table of 5.5 meter. The variation of their results might be caused by the temporal delay of the two data acquisitions and may also depend on seasonal conditions. Nevertheless, I expect to observe the same discontinuity in a depth of approximately 6 meters, resulting in a sudden ascent of the P-wave velocity.

An anomaly, which is intended to be imaged in this thesis, crosses this predominantly depth dependent structure of the subsurface. This anomaly is called "Ettlinger Linie" (EL), but what exactly does this low velocity zone represent and where is its origin? The EL is found to be the remnant of a man made trench serving as defensive line of the early
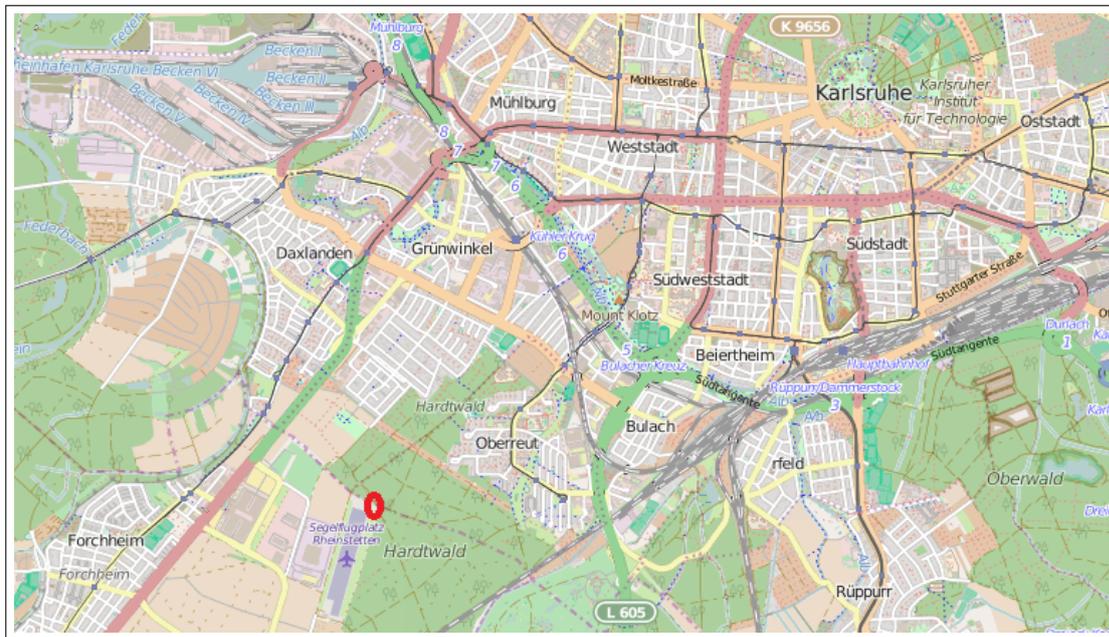
Figure 2.1.: Map of the city of Karlsruhe and the southwestern area. The investigation site is marked by the red circle. Source: OpenStreetMap-contributors *openstreetmap.org*

18th century (Lang, 1907). It was built to defend against the french military forces during the War of the Spanish Succession (1701 - 1714). The section of the EL, which is being investigated, is completely leveled to the ground. However, just tens of meters distant in the adjacent woodland is the trench still visible, which gives a good impression of how the anomaly is supposed to look like. On the basis of the outcrop one can already guess the dimensions of the expected low velocity zone to approximately 10 meters width and 2 meters depth. At what time in history the trench was leveled could not be estimated, which would be a valuable indicator for the degree of re-compaction.

2.2. Acquisition Geometry

Since the Ettlinger Linie is still visible north-west and south-east of the study area and, furthermore, is supposed to form a straight line between these two outcrops (Lang, 1907), one can estimate the pathway accurately. Two independent profiles were aligned orthogonally to the Ettlinger Linie with a distance of about 9.0 meters to each other.

Profile one proceeds from west to east with its origin at source location one (Fig.: 2.2). 71 receivers are used for data acquisition in total. The first receiver is located three meters distant from source location one. Between first receiver and 14th receiver - 16 meters from the origin - geophone spacing is one meter. One meter spacing is also adopted between the 56th receiver - 37 meters distant from the origin - and the 71st receiver, which is located at 52 meters. Between receiver 14 and receiver 56 receiver spacing is reduced to 0.5 meter in order to obtain higher spatial resolution in vicinity of the anomaly. Every two meters

along the profile 28 shots are performed, beginning with a distance to the first receiver of 3.0 meters up to a distance of the last shot to last receiver of 2.0 meters.

Profile two is set up parallel to profile one. Due to regional barriers it is slightly shifted and does not cross the anomaly centered such as profile one does (Fig.: 2.2). Again, 71 receivers are arranged along the profile, beginning west with a distance to first source of 2.0 meters. From first to the 23rd receiver at 24 meters and between the 63rd receiver at 44 meters and the 71st receiver at 52 meters receiver spacing is adapted 1.0 meter. Between receiver 23 and receiver 63 receiver spacing measures 0.5 meter.

A third profile is aligned parallel to the trench in order to record a wave field propagating through undisturbed medium, and serves the purpose of estimating the seismic velocities apart from the Ettlinger Linie. This profile has an extent of 35 meters and an equidistant geophone spacing of 1 meter, that makes a usage of 36 receivers in total. 6 shots are performed along the profile. Assuming the first shot to be the origin and the first receiver is located with an offset of 2 meters, than the shot locations are at 0,4,13,20,27,34 and 43 meters.
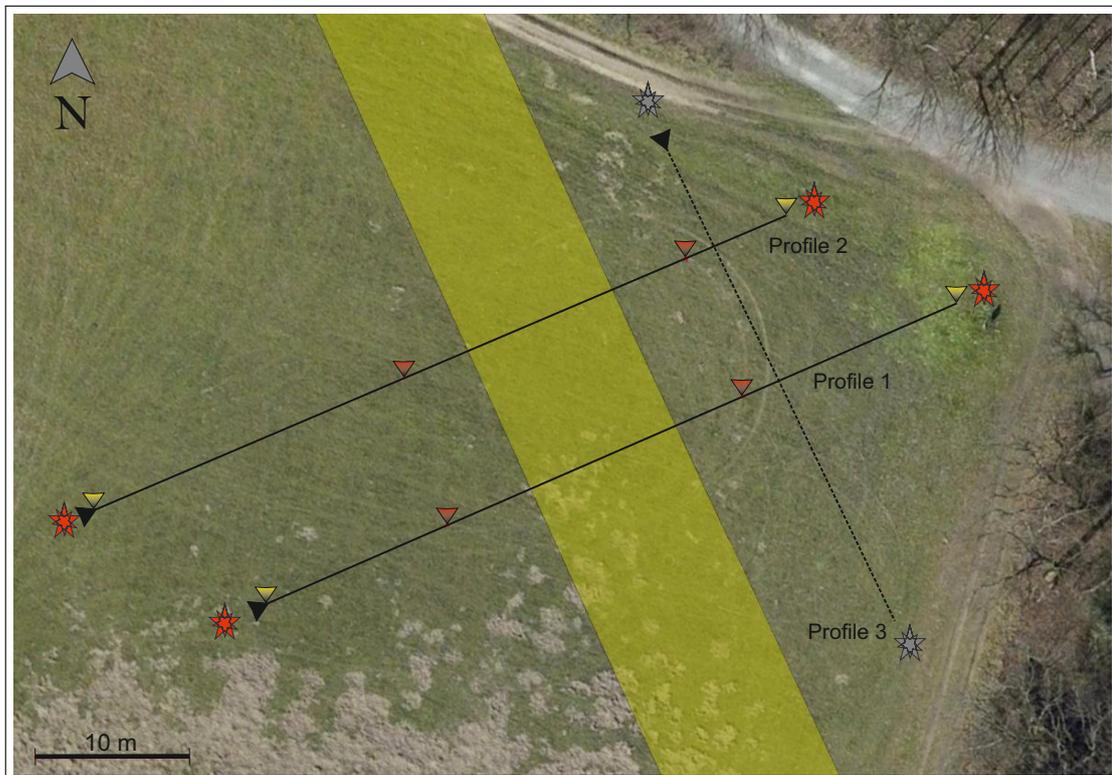

Figure 2.2.: Map of the study area with the anomaly (yellowish area) to be investigated. The black lines mark the profiles, where the geophones are aligned to. The red stars mark the first and last source location for each profile, whilst the black arrows define the shot direction. The receiver spacing is 0.5 meters between the red triangles, whereas receiver spacing is 1.0 meter between red and yellow triangle, each. Profile 3 is sketched with a dashed line, since it is not used for the inversion algorithm and has little meaning. Source: Google, GeoBasis-DE/BKG.

The geophones are equipped with a 4.5 Hz vertical sensor. As source serves a sledge sledge hammer with a weight of about 7.5 kg. Attached to the head of the hammer is an acceleration sensor, which triggers the recording by reaching a certain threshold.

Figure 2.3.: The photo is taken at the study area along profiles one (right) and two (left) in eastward direction. The profiles reach to the fence in the background, each. The geophones are not yet installed

3. Theoretical Background

In this chapter I present a rough explanation of the theoretical background behind the application of full waveform inversion and how the theory is implemented into an numerical inversion code.

3.1. Viscoelastic Wave Propagation

Simulation of the propagation of the seismic wavefield is based upon the theory of linear elasticity, which means that stress is proportional to strain. This relation is formulated by the generelized Hooke's law:

$$\sigma_{ij} = c_{ijkl} \cdot \epsilon_{kl} \tag{3.1}$$

Where σ_{ij} denotes the stress tensor, ϵ_{kl} the strain tensor and c_{ijkl} a functional representing the mechanical properties of the material, usually represented by the stiffness tensor. Repeated indices follow the rule of summation convention in the whole thesis. Introducing following assumptions lead to a simplification of the stress-strain relation (Christensen, 1982):

- Balance of angular momentum (no rotation), implying the symmetry of the stress tensor: $\sigma_{ij} = \sigma_{ji}$

- Displacement of the body continuum is infinitesimal

- The medium properties are isotropic (independent of direction)

The first two restrictions reduce c_{ijkl} from 81 independent parameters to 6 independent parameters. The assumption of an isotropic medium reduces this formula to 2 independent parameters. The so called Lamé constants λ and μ. Hence, the stress strain relation can be defined as:

$$\sigma_{ij} = \lambda \theta \delta_{ij} + 2\mu \epsilon_{ij} \tag{3.2}$$

δ_{ij} denotes the Kronecker delta with the properties $\delta_{ij} = 1$ for $i = j$ and $\delta_{ij} = 0$ for $i \neq j$. This formula represents the purely elastic case with the strain tensor:

$$\epsilon_{ij} = \frac{1}{2}\left(\frac{\partial u_i}{\partial x_j} + \frac{\partial u_j}{\partial x_i}\right) \tag{3.3}$$

and the so called cubic dilatation θ:

$$\theta = \epsilon_{11} + \epsilon_{22} + \epsilon_{33} \tag{3.4}$$

The elastic case, however, is not sufficient describing wave propagation through unconsolidated sediments. There is the need of a proper implementation of the attenuating characteristics of the subsurface in order to account for amplitude decay and dispersion manner of the seismic wave fields. A mathematical solution accounting for viscious behavior is achieved by assuming the lamé constants λ and μ in equation (3.2) to be time dependent and a differentiating them with respect to time. We then receive Λ and M for λ and μ. According to Blanch et al. (1995) equation 3.2 may then be formulated as:

$$\sigma_{ij} = \dot{\Lambda} * \theta \delta_{ij} + 2\dot{M} * \epsilon_{ij} \tag{3.5}$$

With asterisk denoting convolution and the dot time derivative. For the complete derivation of equation (3.5) I refer to Christensen (1982). Blanch et al. (1995) furthermore define $\Pi = \Lambda + 2M$, and take the time derivative of the stress tensor, which then can be expressed by two formulations. One for the diagonal elements and one for the off-diagonal elements:

$$\dot{\sigma}_{ij} = (\dot{\Pi} - 2\dot{M}) * \dot{\theta} + 2\dot{M} * \dot{\epsilon}_{ij} \tag{3.6}$$

$$\dot{\sigma}_{ij} = 2\dot{M} * \dot{\epsilon}_{ij} \tag{3.7}$$

Together with the elastic wave equation (3.8) we obtain a system of formulas fully describing the viscoelastic wave propagation.

$$\rho \frac{\partial v_i}{\partial t} = \frac{\partial \sigma_{ij}}{\partial x_j} + f_i \tag{3.8}$$

With ρ denoting mass density and v_i the seismic phase velocity.

Splitting equation (3.5) into two separate equations is reasonable for the sake of clarity. Henceforth, we can distinguish between a formulation for the viscoelastic wave propagation of acoustic waves (P-waves) (equation 3.6) and shear waves (S-waves) (3.7). Applying the stress relaxation function of a generalized standard linear solid (GSLS), which will be introduced in the following chapter, to the previous formulations yields:

$$\Pi(t) = \pi \Big(1 - \sum_{l=1}^{L} \Big(1 - \frac{\tau_{\epsilon l}^{p}}{\tau_{\sigma l}} \Big) e^{\frac{-t}{\tau_{\sigma l}}} \Big) H(t) \tag{3.9}$$

$$M(t) = \mu \Big(1 - \sum_{l=1}^{L} \Big(1 - \frac{\tau_{\epsilon l}^{s}}{\tau_{\sigma l}} \Big) e^{\frac{-t}{\tau_{\sigma l}}} \Big) H(t) \tag{3.10}$$

With $\pi = \lambda + 2\mu$ and $H(t)$ the Heaviside step function, including the constraint of causality by explicitly setting values with negative time to zero ($H = 0$ for $H(t < 0)$), otherwise the Heaviside function gets one ($H = 1$ for $H(t \geq 0)$). Equations 3.9 and 3.10 have its basis on the assumption that the medium behaves like a viscoelastic system and are called stress relaxation functions. I introduce the generalized standard linear solid in the following section in order to complete the previously mentioned approach.

Generalized Standard Linear Solid

A suitable characterization of a viscoelastic material in terms of stress strain relation is done by the so called standard linear solid (SLS). This model is illustrated by a Maxwell body (dashpot in series with a spring) in parallel with an additional spring. The quality factor $Q(\omega)$ of the SLS is defined as (Aki and Richards, 2002):

$$Q(\omega) = \frac{1 + \omega^2 \tau_\sigma \tau_\epsilon}{\omega(\tau_\epsilon - \tau_\sigma)} \tag{3.11}$$

Where τ_ϵ denotes strain relaxation time and τ_σ denotes strain relaxation time. It is easy to see that the quality factor has a single minimum depending on the choice of the relaxation times. In seismic investigations it is, however, sometimes desirable to assume materials with a rather constant quality factor with respect to frequency. In order to obtain the approximation of a constant quality factor the SLS can be extended to a system of several SLSs in parallel, which may be visualized by a spring in parallel with an array of several Maxwell elements in parallel. Such systems are referred to as generalized standard linear solids (GSLS). This method allows to approximate a constant quality factor over a limited frequency band, as suggested by e.g. Day and Minister (1984) and Blanch et al. (1995). If we define L stress and strain relaxation times for the several GSLS:

$$\tau_{\sigma l} = \frac{\eta_l}{k_{1l}}$$
$$\tau_{\epsilon l} = \eta \frac{k_1 + \sum_{l=1}^{L} k_{2l}}{k_1 \sum_{l=1}^{L} k_{2l}} \tag{3.12}$$

The quality factor of L GSLSs is then defined by:

$$Q(\omega) = \frac{1 - L + \sum_{l=1}^{L} \frac{1 + \omega^2 \tau_{\epsilon l} \tau_{\sigma l}}{1 + \omega^2 \tau_{\sigma l}^2}}{\sum_{l=1}^{L} \frac{\omega(\tau_{\epsilon l} - \tau_{\sigma l})}{1 + \omega^2 \tau_{\sigma l}^2}} \tag{3.13}$$

Blanch et al. (1995) introduce a constant τ (equation 3.14) in order to simplify equation (3.13), and show that the implementation of this constant results only in a magnitude displacement of the quality factor, whereas the shape remains compared to a SLS.

$$\tau = \frac{\tau_{\epsilon l}}{\tau_{\sigma l}} - 1 \tag{3.14}$$

Inserting equation (3.14) into equation (3.13) yields:

$$Q(\omega) = \frac{1 + \sum_{l=1}^{L} \frac{\omega^2 \tau_{\sigma l}^2}{1 + \omega^2 \tau_{\sigma l}^2} \tau}{\sum_{l=1}^{L} \frac{\omega \tau_{\sigma l}}{1 + \omega^2 \tau_{\sigma l}^2} \tau} \tag{3.15}$$

This formulation reduces the adjustable parameters from two per SLS to one parameter plus the variable τ for the estimation of an appropriate quality factor. Furthermore does

this approach reduce computation time due to fewer calculation steps during the forward modeling. The so called τ-method (Blanch et al., 1995) is utilized in the inversion algorithm applied in this thesis. For the sake of integrity, it shall be mentioned that the relaxation times are related to the relaxation frequencies as $f_l = \frac{1}{2\pi\tau_{\sigma l}}$.

3.2. Finite Differences

The partial derivatives of the elastic equations of motion (equation 3.8) have to be transformed into numerical equations in order to suffice the requirements of a computer based numerical solution. This is achieved by a time domain finite difference scheme. A fourth order approximation of the spatial derivative and a second order approximation of the temporal derivative are applied, as suggested by Levander (1988). The implemented forward modeling scheme is developed by Bohlen (1998). The spatial discretization of the subsurface model is realized due to the standard staggered grid (SSG) described by Virieux (1986).

The SSG subdivides a user defined parameter model in a way that additional gridpoints are added in order to calculate the partial derivatives of the elastic wave equation. The values of the partial derivatives of the displacement vectors and the partial derivatives of the density are, therefore, stored between two adjacent gridpoints in horizontal (x) as well as vertical direction (y) (see figure 3.1). Whereas the values of the second-order partial derivatives of the stress tensor with respect to x and y direction are reasonably located between two diagonal gridpoints. The Lamé parameters, density values and the second-order partial derivatives of the stress tensor with respect to x direction as well as the second-order partial derivatives of the stress tensor with respect to y direction are stored at the initially defined gridpoints. To get a closer insight of the spatial discretization used in this thesis I refer to Bohlen (1998), Köhn (2011) and Groos (2013).

Since the parameter ρ_x, ρ_y for the staggered density points and $<\mu>$, denoting the staggered shear modulus, lie in between the predefined grid space (see figure 3.1), they have to be calculated. The shear modulus is averaged harmonically with respect to the four surrounding values and mass density arithmetically with respect to adjacent grid values (Moczo et al., 2004), (Bohlen and Saenger, 2006).

$$< \mu > [j + \frac{1}{2}][i + \frac{1}{2}] = \left(\frac{1}{4}\left(\frac{1}{\mu[j][i]} + \frac{1}{\mu[j][i+1]} + \frac{1}{\mu[j+1][i+1]} + \frac{1}{\mu[j+1][i]}\right)\right)^{-1} \tag{3.16}$$

$$\rho_x[j][i + \frac{1}{2}] = \frac{1}{2}(\rho[j][i+1] + \rho[j][i]) \tag{3.17}$$

$$\rho_y[j + \frac{1}{2}][i] = \frac{1}{2}(\rho[j+1][i] + \rho[j][i]) \tag{3.18}$$

The partial derivatives of the particle displacement u_x in x direction u_{xx} and in y direction u_{xy} are discretized as follows. Indices for the time steps are disregarded in the following equations, for the sake of clarity.
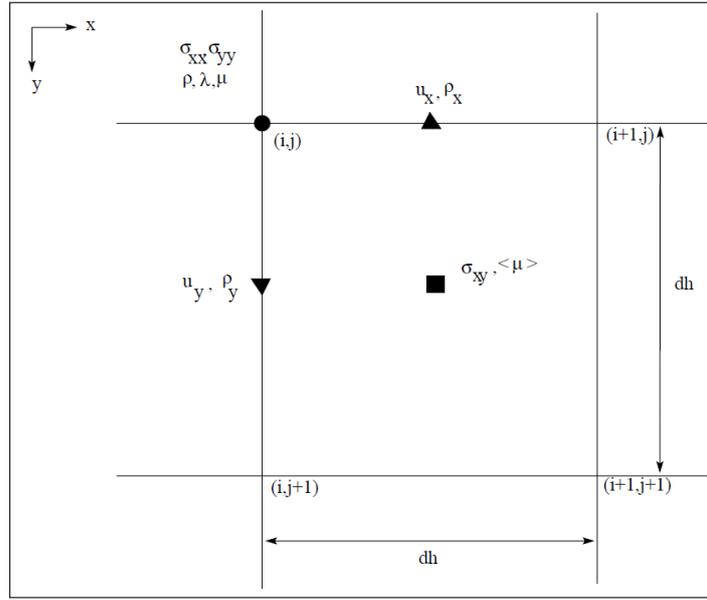
Figure 3.1.: Geometry of the standard staggered grid in two dimensions. Source: Köhn et al. (2013)

$$u_{xx}[j][i] = \frac{u_x[j][i + \frac{1}{2}] - u_x[j][i - \frac{1}{2}]}{dh} \tag{3.19}$$

$$u_{xy}[j + \frac{1}{2}][i + \frac{1}{2}] = \frac{u_x[j + 1][i + \frac{1}{2}] - u_x[j][i + \frac{1}{2}]}{dh} \tag{3.20}$$

The formulation for the partial differentiation of the y-component of the displacement with respect to y ($u_{yy}[j][i]$) is obtained by substituting $u_x[j][i + \frac{1}{2}]$ and $u_x[j][i - \frac{1}{2}]$ with $u_y[j + \frac{1}{2}][i]$ and $u_y[j - \frac{1}{2}][i]$ in equation (3.19), respectively. For the formulation of u_{yx} one has to substitute $u_x[j + 1][i + \frac{1}{2}]$ and $u_x[j][i + \frac{1}{2}]$ with $u_y[j + \frac{1}{2}][i + 1]$ and $u_y[j + \frac{1}{2}][i]$ in equation (3.20), respectively. The discretized form of the linear elastic stress strain relations are then written as:

$$\sigma_{xy}[j + \frac{1}{2}][i + \frac{1}{2}] = <\mu>[j + \frac{1}{2}][i + \frac{1}{2}]\left(u_{xy}[j + \frac{1}{2}][i + \frac{1}{2}] + u_{yx}[j + \frac{1}{2}][i + \frac{1}{2}]\right) \tag{3.21}$$

$$\sigma_{xx}[j][i] = \lambda[j][i] * \left(u_{xx}[j][i] + u_{yy}[j][i]\right) + 2* <\mu>[j][i] * u_{xx}[j][i] \tag{3.22}$$

$$\sigma_{yy}[j][i] = \lambda[j][i] * \left(u_{xx}[j][i] + u_{yy}[j][i]\right) + 2* <\mu>[j][i] * u_{yy}[j][i] \tag{3.23}$$

Subsequently, we can define the second order partial derivatives utt_x and utt_y of the displacement with respect to time as follows. The index n is introduced to emphasize the dependence on time:

$$utt_x^n[j][i + \frac{1}{2}] = \sigma_{xx}[j][i + 1] - \sigma_{xx}[j][i] + \sigma_{xy}[j + \frac{1}{2}][i] - \sigma_{xy}[j - \frac{1}{2}][i] \qquad (3.24)$$

$$utt_y^n[j + \frac{1}{2}][i] = \sigma_{xy}[j][i + \frac{1}{2}] - \sigma_{xy}[j][i - \frac{1}{2}] + \sigma_{yy}[j + 1][i] - \sigma_{yy}[j][i] \qquad (3.25)$$

This leads finally to the momentum equation:

$$u_x^{n+1}[j][i + \frac{1}{2}] = 2 * u_x^n[j][i + \frac{1}{2}] - u_x^{n-1}[j][i + \frac{1}{2}] + \frac{dt^2}{dh * \rho_x[j][i + \frac{1}{2}]} * utt_x^n[j][i + \frac{1}{2}]$$

$$(3.26)$$

$$u_y^{n+1}[j + \frac{1}{2}][i] = 2 * u_y^n[j + \frac{1}{2}][i] - u_y^{n-1}[j + \frac{1}{2}][i] + \frac{dt^2}{dh * \rho_y[j + \frac{1}{2}][i]} * utt_y^n[j + \frac{1}{2}][i]$$

$$(3.27)$$

3.3. Rayleigh Waves

The observed seismic signals are highly dominated by surface waves, to be more precisely by Rayleigh waves. Therefore, most information of the subsurface is extracted by the amplitude fitting of these types of waves. Generally speaking, Rayleigh waves are the result of a superposition of P-waves and S-waves propagating along the boundary of a solid and a free surface. To get a first impression of the abilities inverting for Rayleigh waves I introduce the solutions of the equations of motion for Rayleigh waves. The following equations are adopted from Aki and Richards (2002), who assumes plane waves interacting (transmission or reflection) with a boundary of a homogeneous half-spaces and a free surface. Depending on the incident angle, the plane wave field can be transformed into a wave field traveling along the boundary. If we assume that the wave propagates along the boundary with a velocity of c_R and the shear phase velocity v_s as well as the acoustic phase velocity v_p of the homogeneous half-space are related such that:

$$v_p > v_s > c_R \qquad (3.28)$$

with c_R the propagation velocity of the Rayleigh wave. Aki and Richards (2002) use the notation horizontal slowness $p = \frac{1}{c_R}$ instead of velocity. We then formally get:

$$P = \hat{P} \left(\frac{v_p p}{i\sqrt{v_p^2 p^2 - 1}} \right) e^{-\omega \sqrt{p^2 - \frac{1}{v_p^2}} z} e^{i\omega(px - t)}$$

$$(3.29)$$

$$S = \hat{S} \left(\frac{i\sqrt{v_s^2 p^2 - 1}}{-v_s p} \right) e^{-\omega \sqrt{p^2 - \frac{1}{v_s^2}} z} e^{i\omega(px - t)}$$

The first equation describes the wave propagation of the acoustic component of the Rayleigh wave with a maximum displacement amplitude at the surface ($z = 0$) of $\hat{P}$. The subsequent vector denotes a unit vector such that

$$(v_p p)^2 + \left(i\sqrt{v_p^2 p^2 - 1}\right)^2 = 1 \tag{3.30}$$

We receive two separate equations describing the P-component of the Rayleigh wave and the SV-component. Aki and Richards (2002) call this kind of wave inhomogeneous, since it is necessary to introduce a complex amplitude from the condition (equation 3.28). The third factor in equation (??) accounts for the depth (z), assuming that we have an exponential amplitude decay. The last factor describes the phase with offset x and time t. The formula below is the solution of the shear component of Rayleigh waves. The elements can be interpreted analogous as the elements for the acoustic equation.

We can extract the following rules for Rayleigh waves from equations (3.29):

- The waves decay exponentially with distance from the surface

- P- and SV-component decrease independently from each other with depth

- The particle motion at the free surface is retrograde elliptical

- The particle motion is prograde elliptical below a certain depth depending on frequency

Assuming a free surface boundary condition, where the stress vanishes ($\sigma_{zz} = \sigma_{zx} = 0$) for ($z = 0$) leads to the Rayleigh function:

$$R(p) = \left(\frac{1}{v_s^2} - 2p^2\right)^2 - 4p^2 \sqrt{p^2 - \frac{1}{v_p^2}} \sqrt{p^2 - \frac{1}{v_s^2}} = 0 \tag{3.31}$$

We can conclude by the Rayleigh function that the velocity of the Rayleigh wave must be slower than the P- as well as the S-wave velocity.

3.4. Full Waveform Inversion

Full waveform inversion aims to minimize the misfit of observed and synthetic data during an iterative process, in which the model parameters are updated, such that the forward simulated wave field, and therefore the obtained synthetic signals, resemble the observed seismic signals better. generated by a forward modeling code (see section 3.2) simulating the seismic wave field. During an iterative process the subsurface model parameters are updated in each iteration step which include seismic wave velocities (P- and S-waves) as well as density in order to obtain a best fit subsurface model, finally.

In the beginning one has to guess an initial model, which is supposed to define the real subsurface as close as possible. Hence, a priori information about the investigation area is desirable. It is crucial to find a model that prevents a deviation of the synthetic

seismograms to the real seismograms of more than half a cycle, otherwise the model is updated in the opposed direction and the final model gets a solution of a local minimum. The shift of a synthetic wave cycle to an adjacent wave cycle of the real data is known as cycle-skipping. In order to avoid these phase shifts the inversion algorithm starts off with a low frequency data set and proceeds stepwise to higher frequencies, when the data misfit can not be decreased by a certain threshold, as suggested by Bunks et al. (1995). In each iteration step the gradient of the data misfit is estimated by the adjoint approach introduced by Tarantola (1984) and the direction of the gradient is calculated via a conjugate gradient method (see section 3.4.2). The model parameters density, S- and P-wave velocity are then updated in negative direction of the gradient with a predefined step length. The step length estimation for the model update is described in section 3.4.3. The updated model replaces the initial model and the previously sketched processes are repeated. The progress of the full waveform inversion is visualized as a flow chart in figure (3.2).

The full waveform inversion code was originally designed by Köhn (2011). The inversion algorithm is named "subwavelength DEtail resolving Nonlinear Iterative SEismic inversion" (DENISE).
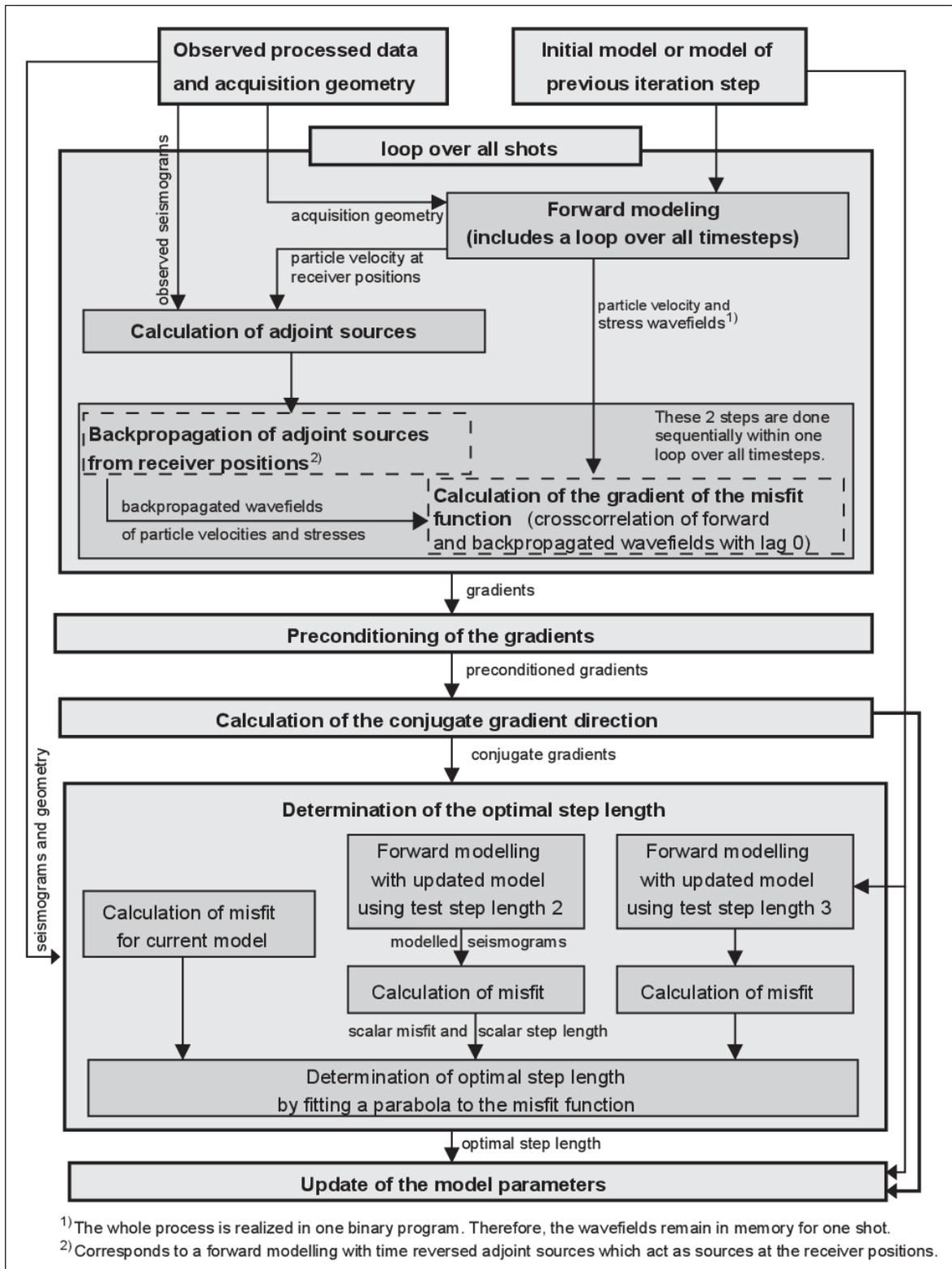
Figure 3.2.: Flow chart of the calculations performed during one iterative process in DENISE. Source:(Groos, 2013).

3.4.1. Misfit Definition

As basis of the inversion process I introduce the misfit function as it is applied in this work. A common approach of estimating the misfit E is done by the so called least squares norm $|L|_2$ of the difference of synthetic $\vec{u}^{synth}$ and observed displacement seismograms $\vec{u}^{obs}$.

$$E = |L|_2 = \sum_{s}^{ns} \sum_{r}^{nr} \delta \vec{u}_{s,r}^{T} \delta \vec{u}_{s,r} = \sum_{s}^{ns} \sum_{r}^{nr} |\delta \vec{u}_{s,r}|^2 \qquad (3.32)$$

With the vector $\delta \vec{u} = \vec{u}^{synt} - \vec{u}^{obs}$ containing the residuals of each time sample and T denoting the transpose of a vector. The misfit is summed over the number of sources ns and the number of receivers nr. This approach allows the misfit to be defined as the entire residual elastic energy.

The misfit definition can be extended by dividing the data by their corresponding quadratic mean and yields the the definition of the least squares norm of the normalized wavefields (Choi and Alkhalifah, 2012)

$$E = \sum_{s}^{ns} \sum_{r}^{nr} \left| \frac{\vec{u}_{s,r}^{synt}}{|\vec{u}_{s,r}^{synt}|} - \frac{\vec{u}_{s,r}^{obs}}{|\vec{u}_{s,r}^{obs}|} \right|^2 \qquad (3.33)$$

The applied misfit used in the inversion algorithm is slightly modified by an additional normalization (Groos, 2013) of the whole term with respect to the number of sources and receivers:

$$E = \frac{1}{n_s n_r} \sum_{s}^{ns} \sum_{r}^{nr} \left| \frac{\vec{u}_{s,r}^{synt}}{|\vec{u}_{s,r}^{synt}|} - \frac{\vec{u}_{s,r}^{obs}}{|\vec{u}_{s,r}^{obs}|} \right|^2 \qquad (3.34)$$

The big advantage of the use of the normalized wavefields is that far offset traces are accounted for as much as the near offset traces. The drawback is that the information of the amplitude ratio with offset is lost.

3.4.2. Gradient Calculation

Denise deploys an adjoint approach to calculate the gradient of the misfit function (Tarantola, 1984). This approach is realized by backpropagating the residuals of observed and synthetic seismograms from the receiver position in time and applying a zero-lag cross-correlation to this wavefield and the observed forward propagating wavefield.

For the derivation of the gradient direction I refer to Köhn (2011). The formulations, however, are originally related to Tarantola (1988) and Aki and Richards (2002). First of all I calculate the differentiation of the misfit function declared in equation (3.35). The misfit function can be rewritten in integral form

$$E = \frac{1}{n_s n_r} \sum_{s}^{ns} \int dt \sum_{r}^{nr} \left(\hat{u}_{s,r}^{synt}(x_s, x_r, t) - \hat{u}_{s,r}^{obs}(x_s, x_r, t) \right)^2 \qquad (3.35)$$

Where $\hat{u}^{synt}$ and $\hat{u}^{obs}$ are the normalized seismograms of the modeled data and the observed data, respectively. The derivation of the misfit function with respect to the model parameters m yields

$$\frac{\partial E}{\partial m} = \frac{2}{n_s n_r} \sum_s^{ns} \int dt \sum_r^{nr} (\hat{u}^{synt}_{s,r}(x_s, x_r, t, m) - \hat{u}^{obs}_{s,r}(x_s, x_r, t)) \frac{\partial \hat{u}^{synt}_{s,r}(x_s, x_r, t, m)}{\partial m} \tag{3.36}$$

Since only $\hat{u}^{synt}$ depends on the model parameters m. The goal is now to estimate the Frechét derivative $\frac{\partial \hat{u}^{synt}_{s,r}}{\partial m}$. This can be achieved by the assumption of perturbations in the model space m (Tarantola, 1988). First of all I define the equations of motion for the viscoelastic case.

$$\rho \frac{\partial^2 u_i}{\partial t^2} - \frac{\partial \sigma_{ij}}{\partial x_j} = \phi_i \tag{3.37}$$

$$\sigma_{ij} - \int dt' \Psi_{ijkl} \frac{\partial u_k}{\partial x_l} = M_{ij} \tag{3.38}$$

The perturbations in the model space can be expressed as

$$\rho \rightarrow \rho + \delta\rho$$
$$\sigma_{ij} \rightarrow \sigma_{ij} + \delta\sigma_{ij}$$
$$\Psi_{ijkl} \rightarrow \Psi_{ijkl} + \delta\Psi_{ijkl}$$

resulting in a perturbation of the displacement field

$$u_i \rightarrow u_i + \delta u_i \tag{3.39}$$

Inserting these formulations in equations (3.37) leads to

$$\rho \frac{\partial^2 u_i}{\partial t^2} - \frac{\partial \sigma_{ij}}{\partial x_j} + \rho \frac{\partial^2 \delta u_i}{\partial t^2} + \delta\rho \frac{\partial^2 u_i}{\partial t^2} + \delta\rho \frac{\partial^2 \delta u_i}{\partial t^2} - \frac{\partial \delta\sigma_{ij}}{\partial x_j} = \phi_i$$

$$\sigma_{ij} + \delta\sigma_{ij} - \int dt' \Psi_{ijkl} \frac{\partial u_k}{\partial x_l} + \delta\Psi_{ijkl} \frac{\partial u_k}{\partial x_l} + \Psi_{ijkl} \frac{\partial \delta u_k}{\partial x_l} + \delta\Psi_{ijkl} \frac{\partial \delta u_k}{\partial x_l} = M_{ij}$$

Assuming the perturbations are small, then the quadratic terms of the perturbation can be neglected. Furthermore, we can distinguish between the initial wavefield (see equation 3.37) and the wavefield of the residuals. The residual wavefield is then described by the system of equations

$$\rho \frac{\partial^2 \delta u_i}{\partial t^2} - \frac{\partial \delta\sigma_{ij}}{\partial x_j} = -\delta\rho \frac{\partial^2 u_i}{\partial t^2}$$

$$\delta\sigma_{ij} - \int dt' \Psi_{ijkl} \frac{\partial \delta u_k}{\partial x_l} = \int dt' \delta\Psi_{ijkl} \frac{\partial u_k}{\partial x_l}$$

With the so called secondary Born sources $\delta\phi$ and δM (Tarantola, 1988).

$$\delta\phi_i = -\delta\rho \frac{\partial^2 u_i}{\partial t^2}$$
$$\delta M_{ij} = \int dt' \delta\Psi_{ijkl} \frac{\partial u_k}{\partial x_l}$$

In order to find a solution for the perturbed wave field δu the Green function is introduced.

Green function

A very generous description of the Green function is presented here, for more details I refer to Aki and Richards (2002) on whom the derivation relies on.

The elastodynamic Green function might be explained as the impulse response of the subsurface. More explicitly, it represents the displacement field at any arbitrary position x in the model space and time t if a unit impulse at location x_s and time τ is performed in the n-direction. The i-th component of the displacement can then be denoted as $G_{in}(x,t;x_s,\tau)$.

$$\rho \frac{\partial^2}{\partial t^2} G_{in} - \frac{\partial}{\partial x_j}\left(c_{ijkl}\frac{\partial}{\partial x_l}G_{kn}\right) = \delta_{in}\delta(x-x_s)\delta(t-\tau) \qquad (3.40)$$

The right hand side of this equation describes a unit impulse where δ_{in} is the Kronecker Delta and $\delta(x-x_s)$ as well $\delta(t-\tau)$ are Dirac delta functions with the property $\delta(0) = 1$ and $\delta(\neq 0) = 0$ otherwise. If we assume the boundary conditions being independent of time, then we can choose the time origin.

$$G(x,t;x_s,\tau) = G(x,t-\tau;x_s,0) = G(x,-\tau;x_s,-t) \qquad (3.41)$$

Additionally, it can be assumed that the material properties are independent of time concluding to a space-time reciprocity

$$G_{nm}(x,t;x_s,\tau) = G_{mn}(x_s,-\tau;x,-t) \qquad (3.42)$$

The space-time reciprocity is mandatory for the formulation of the residual wave field. This theorem states that the response at point x in n-direction generated by a source at location x_s is identical to the response at point x_s in m-direction generated by a source at location x_s (Tarantola, 1988). Subsequently, the perturbated displacement field δu_i can be formulated according to Aki and Richards (2002)

$$\delta u_i(x,t) = \int_V dV \int_0^T dt' G_{ij}(x,t;x',t')\delta\phi_j(x',t') - \int_V dV \int_0^T dt' \frac{\partial G_{ij}}{\partial x'_k}(x,t;x',t')\delta M_{jk}(x',t')$$

$$(3.43)$$

3.4.3. Step Length Estimation

To what degree the model update is performed relies on the predefined step length. The step length is defined by a factor μ scaling the gradient direction $\frac{\partial E}{\partial m}$ such that the model parameters m_{n+1} are updated as shown in equation (3.44).

$$m_{n+1} = m_n - \mu P_n \left(\frac{\partial}{\partial m} \right)_n \qquad (3.44)$$

Where n is the index for each model parameter and P is an additional preconditioning operator such as a gradient filter (see 5.4). This equation defines the model update for one single iteration step. The applied inversion algorithm calculates the step length due to a parabolic line search algorithm (Köhn et al., 2013). The line search algorithm estimates the misfit for several step lengths and fits a parabolic curve (figure 3.3).
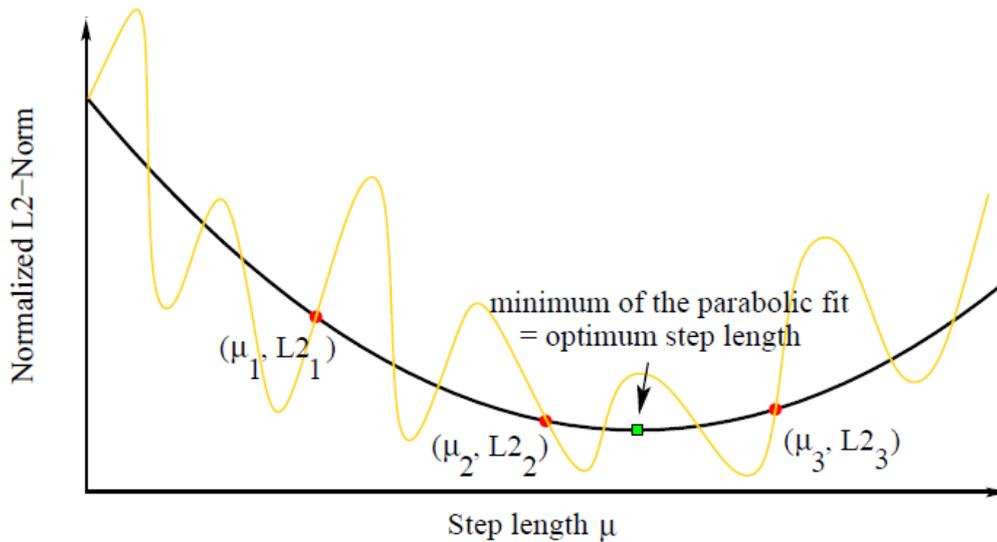
Figure 3.3.: Parabolic line search algorithm. The red dots denote the calculated misfit values as functions of the various step lengths μ_1, μ_2 and μ_3. The yellow curve is a sketch of the misfit function. The green mark is the minimum of the fitted parabola. Source: (Köhn et al., 2013)

Since the estimation of various step lengths can be time consuming I apply the minimum of three. In the case that the line search fails, for example if the parabolic curvature is negative with respect to the misfit, the predefined step length is divided by a fixed value and restarts the process. I choose a rather too small value for the step length's estimation for a certain reason. The degree of model update is determined for all three parameters (density, S- and P-wave velocity) in the same manner. If the step length exceeds a certain threshold the inversion might get unstable and fails. The drawback of a small step length is the risk of getting stuck in a local minimum.

The inversion algorithm DENISE makes use of the conjugate gradient method. This method is applied in order to speed up the convergence speed. The conjugate gradient remembers the previous direction of misfit reduction δm_{n-1} and accounts for it in the following iteration step:

$$m_{n+1} = m_n + \mu_n(\delta m_n + \beta_n \delta m_{n-1}) \tag{3.45}$$

4. Field Data

The seismic signals are acquired via three different profiles. The data from profile one and profile two serve the application of the full waveform inversion itself, which is described in chapter 5. The measurements of profile three is originally performed in order to estimate the subsurface structure distant from the Ettlinger Linie, where only depth-dependent subsurface variations are presumed. This chapter focuses on a check of the data quality as well as on the first processing steps to enable full waveform inversion.

4.1. Data acquisition

The seismic signals are measured via one-component geophones, which convert the vertical ground velocity proportionally into voltage in the desired frequency band. The geophones are equipped with a vertical sensor with a natural frequency of 4.5 Hz, which is sufficient, since the desired signals are supposed to contain frequencies above 10 Hz. As datalogger serve geodes from geometrics with 24 channels. In order to connect 71 geophones in a row, a sum of three geodes have to be used. The sampling interval is set to 0.5 ms, which seems a bit exaggerating, considering that the significant signals don't exceed 100 Hertz and, according to the Nyquist criterion, signals containing frequencies below 1000 Hz can still be observed with this sampling rate. Nevertheless, memory space is not wasted, because the data has to be upsampled prior to FWI to satisfy the Courant-Friedrichs-Lewy criterion described in section (4.3), anyway. The total recording time of each trace is originally 2.0 seconds, which is decreased to 0.45 seconds in order to reduce computing time during the inversion process.

The investigation area exhibits comfortable experimental conditions in terms of seismic data surveys. The closest frequented street is more than one kilometer distant and the gliding airfield of Rheinstetten is adjacent to woodland. One could claim that seismic noise might be induced by the coupling of wind and forest, but at the time of the running measurements wind was very rare. Nevertheless, the seismic traces are stacked five times for each shot in order to enhance signal to noise ratio.

4.2. Quality control

This chapter focuses on a rough quality control of the acquired data. A more detailed adjustment of the observed data is illustrated in section (5.4). First of all, it has to be mentioned that the first trace of profile one as well as profile two are numb. This circumstance is caused by my own fault and misinterpretation of the set-up of the software and couldn't be fixed until profile three. Therefore, only 71 of the 72 available receivers are properly

functioning. The first trace is cut out and causes a shift in the first offset from 2 meters, as initially intended, to 3 meters (see section 2.2). Furthermore, the geophones closest to the source, usually with a distance shorter than 1.5 meters, are overdriven and become highly non-linear. These traces must be neglected during the inversion, which can be accomplished via so called 'trace killing' shot by shot. For visual illustration the traces of profile one, shot number 5 are plotted in figure (4.1). No filters are applied on this shot section at all, but one can easily detect the overdriven seismic trace at 8 meters, revealing a signal with the geophones' natural period of about 0.22 seconds.

(a)   (b)
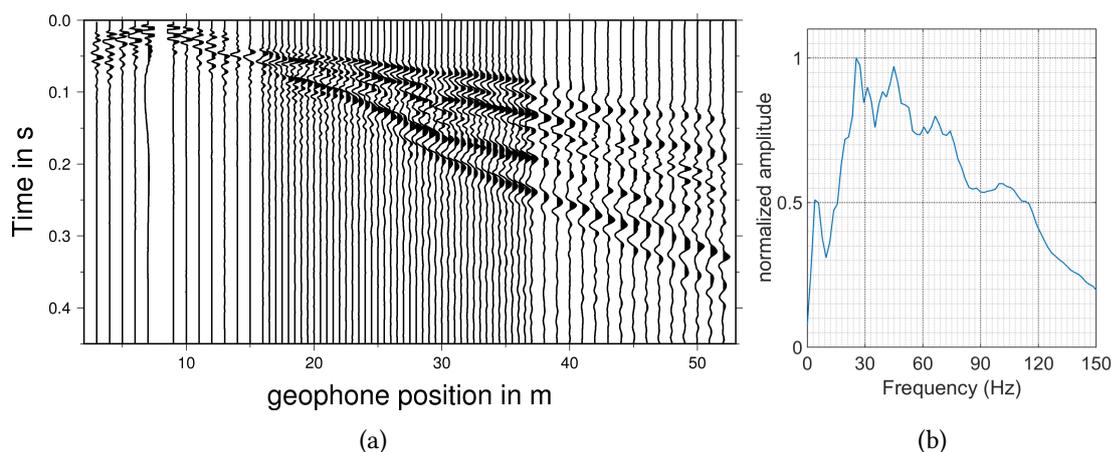
Figure 4.1.: Shot section of source number 5 showing the raw seismic traces (a) and the corresponding normalized amplitude spectrum (b). The traces are normalized by their maximum amplitude.

(a)   (b)
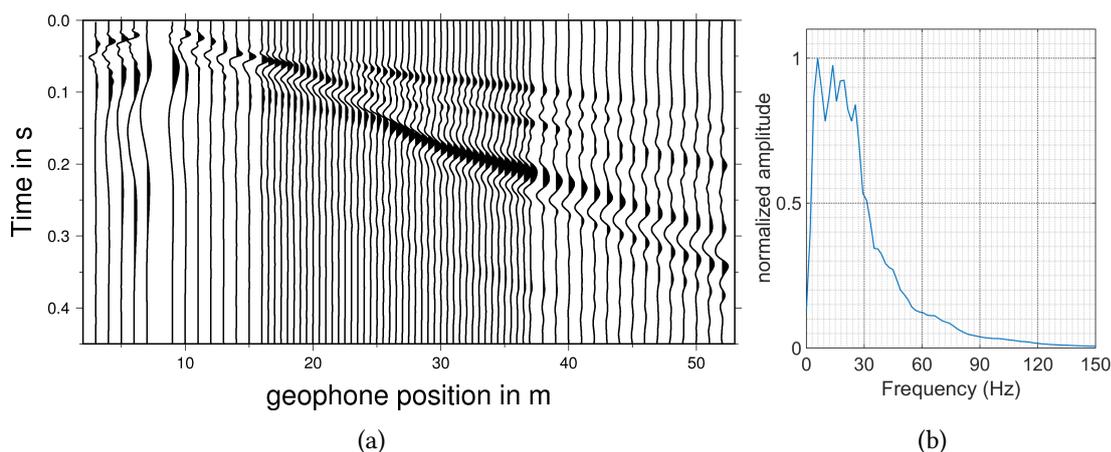
Figure 4.2.: Shot section of source number 5. The seismic traces are filtered with a second order low-pass Butterworth filter with a corner frequency of 5 Hz (a) and the corresponding normalized amplitude spectrum (b). Again, the traces are normalized by their maximum amplitude.

It is recommended to have a look at the seismograms filtered with a low-pass filter with the cutoff frequency of the lowest value deployed in the inversion in order to estimate corrupted traces, which might not be visible without filtering.

4.3. Data Preprocessing

In this chapter I describe the very basic steps that have to be applied, in order to run a two-dimensional full waveform inversion, no matter what the observed seismic traces might look like. Therefore, I do not go too much into detail with respect to my own observed data in this chapter.

4.3.1. Resampling and Courant instability

The measured data has to be customized in order to guarantee stability in the forward modeling process. One important consideration concerns the so called Courant-Friedrichs-Lewy criterion (Courant et al., 1928). It describes the threshold of the minimum temporal sampling rate of the measured data applicable (equation 4.1). It is highly recommended to upsample ones data with a convenient distance to this threshold if necessary, otherwise the forward modeling might get unstable and the inversion will be terminated.

$$dt \leq \frac{dh}{h\sqrt{2}v_{max}} \tag{4.1}$$

Where dt denotes temporal discretization, dh spatial discretization of the subsurface model, h a factor depending on the order used in the finite difference scheme and v_{max} is the maximum phase velocity. Referring to the initial model used for the inversion in this thesis with the values $v_{max} = 1836.0\frac{m}{s}$, $dh = 0.1m$ and a factor $h = \frac{7}{6}$, belonging to a fourth order taylor series approximation, dt must not exceed $0.033ms$. This value is an approximation, since the seismic velocities specified in the initial model do not account for the dispersive material properties yet. Hence, the real maximum phase velocity may slightly differ (Köhn et al., 2013). Nevertheless, to ensure stability during the inversion, the observed data is upsampled to a time discretization of $0.025ms$.

4.3.2. 3D-2D Transformation / Line Source Simulation

Due to the two-dimensional forward modeling code the obtained data must be transformed from its three-dimensional propagation characteristics into two-dimensional propagation characteristics. This method is also called line-source simulation, implying that the real source signal in the field, acting as a point source, must be transferred into a line source, which is perpendicular to the path of the aligned geophones and has infinite extent. The processing steps of the 3d-to-2d transformation are completely adopted from Forbriger et al. (2014).

Most obviously, surface waves propagating through a homogeneous three-dimensional space suffer a higher amplitude decay than propagating in a two-dimensional space due to geometrical spreading. Furthermore, the geometry of a line source differs from a point

source, such that the traveling distance of the wave field increases along the line source (see 4.3), that is in y-direction. Resulting in a phase shift of the signals measured at the receiver positions.
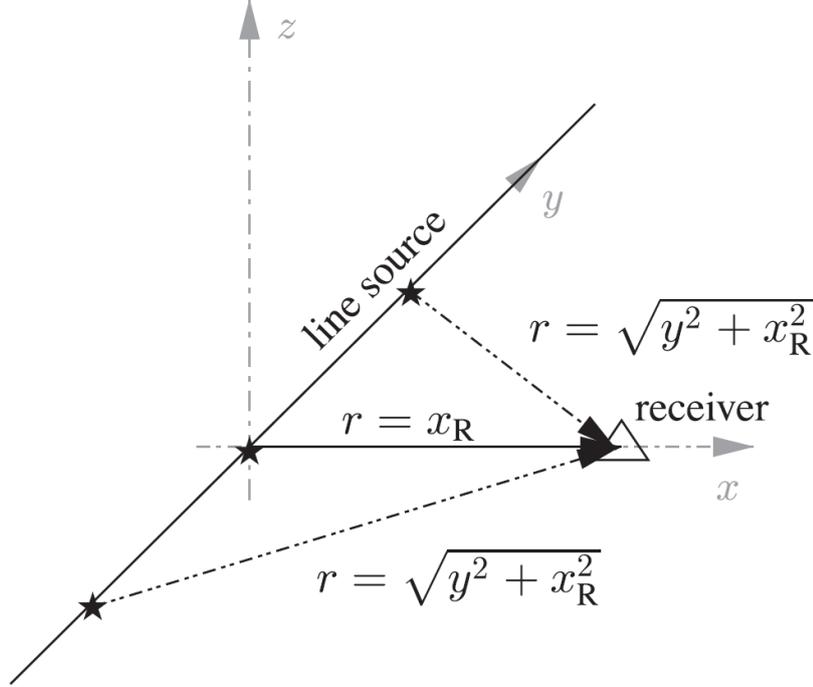

Figure 4.3.: Sketch of the geometrical illustration of the line source. x_r denotes the receiver position, r is the distance of each point of the line source to the receiver location and y denotes the point of the line source. Source: Forbriger et al. (2014)

The amplitude correction is achieved by the factor:

$$F_{amp} = \sqrt{2r_{off}v_{ph}} \tag{4.2}$$

With phase velocity v_{ph}. Since surface waves propagate approximately along the same path as direct waves, the offset r_{off} can be assumed to equal the propagation path. Concluding phase velocity v_{ph} to be defined as:

$$v_{ph} = \frac{r_{off}}{t} \tag{4.3}$$

With t denoting traveltime. Then we get:

$$F_{amp} = r_{off}\sqrt{2}\sqrt{\frac{1}{t}} \tag{4.4}$$

In order to achieve a simulation of surface waves propagating in a two-dimensional plane, the following processes are performed:

- convolution of the waveforms with $\sqrt{\frac{1}{t}}$

- application of a time-domain taper of $\sqrt{\frac{1}{t}}$

- multiplication of the waveforms with $\sqrt{2}r_{off}$

5. Field Data Application

In this chapter I introduce the most relevant parameters to be adjusted prior to inversion, as well as the choice of an appropriate initial model and, last but not least, the essential steps of data pre-processing in order to guarantee successful modeling. I want to point out that it is desired to apply as less data adjustment as possible in order to ensure model update originating from the real data fitting and not from manipulated data. Nevertheless, certain steps have to be performed to circumvent instabilities. It is abandoned to implement the anomaly described in chapter 2 in the initial model, The focus lies on reconstructing this anomaly.

5.1. Initial Model

The choice of a suitable initial model is crucial for a successful inversion. Suitable means in this case that cycle skipping must be prevented.

The p-wave velocity model is obtained via seismic refraction theory. Profile three is assumed to be set up over a nearly lateral homogeneous subsurface structure distant from the 'Ettlinger Linie'. Therefore, the data acquired at these Profiles are more suitable for a straightforward v_p estimation rather than Profile 1 btw. Profile 2.

A discontinuity is located at a depth of 5.97 meters, seperating a homogeneous layer with a seismic P-wave velocity v_p of 364.0 meters per second and an underlaying homogeneous half space with a seismic velocity of 1836.0 meters per second. During the first approaches of FWI it has turned out that sharp discontinuities of the one-dimensional initial model prevents model parameter updates in greater depths. Hence, the discontinuity of the presumed groundwater table is modeled via a high gradient layer of 0.4 meter breadth, reaching from a depth of 5.8 meters to 6.2 meters, but does not exhibit the expected results.

The depth dependent s-wave velocities are adopted by Lisa Groos (Groos, 2013), who investigated the same study area. Groos (2013) applied FWI successfully by deploying an one-dimensional (depth dependent) initial model with a layer overlaying a homogeneous half space. The shear-wave velocities v_s of the layer increases from 100 meters per second at the surface of the model to a depth of nine meters with 369 meters per second linearly. The homogeneous halfspace beyond 9 meters is parameterized by a constant S-wave velocity v_s of 369 meters per second. The parameterization of the initial model are displayed once more in the following table:

depth in m	v_p in $\frac{m}{s}$	v_s in $\frac{m}{s}$	ρ in $\frac{kg}{m^3}$
0.0	364.0	100.0	1700.0
5.8	364.0	273.4	1700.0
6.2	1836.0	285.3	2000.0
9.0	1836.0	369.0	2000.0
16.0	1836.0	369.0	2000.0

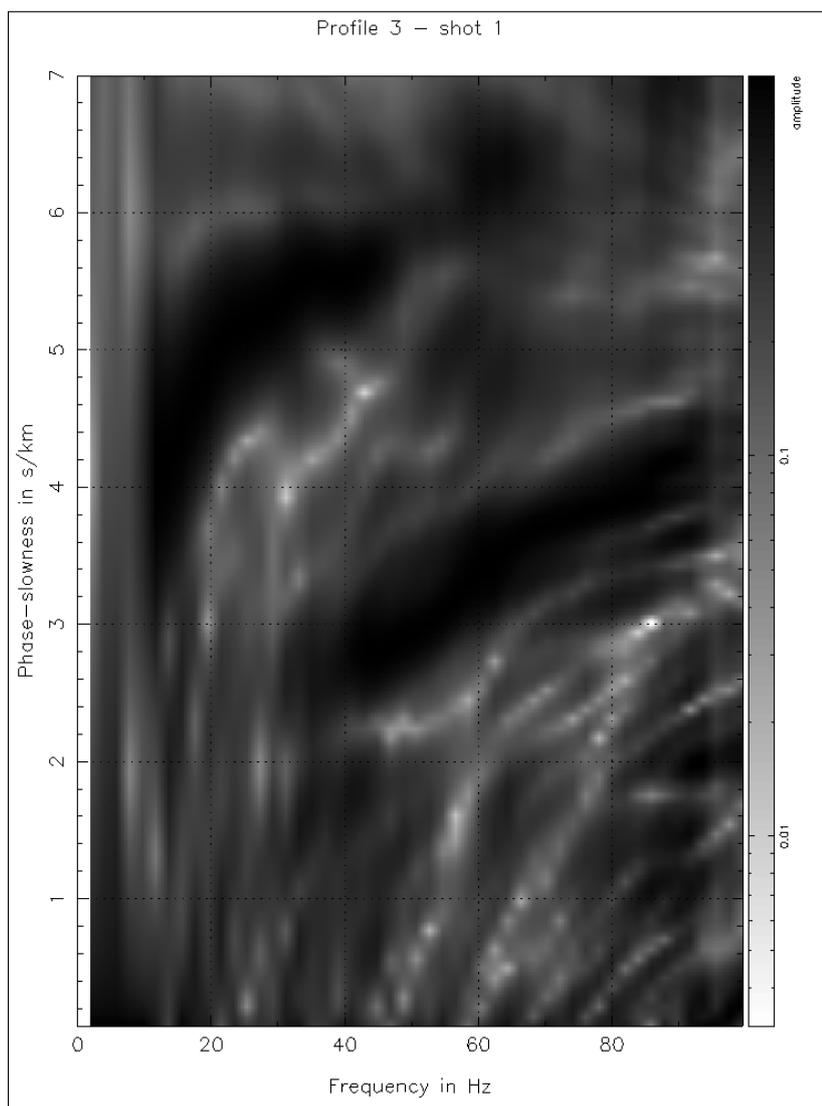Table 5.1.: The table shows the model spaces of the initial model used for the inversion

Figure 5.1.: This figure shows the dispersion curve of profile three. Two modes of the Rayleigh wave can be distinguished. The presumed fundamental Rayleigh mode arises from 5 Hz and reaches to 50 Hz. The observed phase velocities of the fundamental mode lie in between 160 and 250 meters per second. A higher mode is visible in the frequency range of 40 to 95 Hz. The phase velocities reach from 220 to 400 meters per second.

5.2. Estimation of Quality factor

Since the quality factor is handled as a fixed parameter in DENISE, it must be estimated prior to inversion, and will stay untouched during the inversion. Previous studies assume that the quality factor is independent of frequency in the desired frequency band of 10 to 80 Hertz (e.g. Blanch et al. (1995)). Groos (2013) performs viscoelastic FWI choosing a nearly constant quality factor and proves this approach to be reasonable. Nevertheless, I determine the quality factor according to Jeng et al. (1999), who suggest the use of a frequency dependent quality factor. The quality factor can be estimated by the amplitude decay with offset:

$$ln\frac{S_1(Z_1, f)}{S_2(Z_2, f)} = C + \frac{\pi f \Delta Z}{Qv} \tag{5.1}$$

With $\Delta Z = Z_2 - Z_1$

Where $S_1(Z_1, f)$ and $S_2(Z_2, f)$ are the Fourier amplitude spectra at location Z_1 and Z_2, respectively. ΔZ is the offset of two receiver locations and C is a constant accounting for geometric divergence as well as source and receiver functions. f declares frequency, v is the seismic wave velocity and Q is the desired quality factor. In order to define an appropriate frequency dependent quality factor the recorded data is filtered with a bandpass of 10 Hertz in the frequency range of 10 to 80 Hertz. The natural logarithm of the obtained amplitude spectra are then individually plotted against the offset and a linear regression model is determined (Fig.: 5.2). The slope of the regression line is defined by $\pi f/Qv$. The seismic wave velocity of a given frequency band is estimated from the frequency-slowness spectrum (Fig.: 5.1) and causes the biggest part of error in terms of standard deviation, especially at low frequencies from 10 to 20 Hz and from 20 to 30 Hz. The calculated quality factor is shown in Figure 5.3. The quality factor applied in DENISE is constructed due to three relaxation mechanisms ($L_1 = 0.01$, $L_2 = 80.0$, $L_3 = 100.0$) with a value of τ of 0.1. The appropriability is proven by comparing the data misfit of the stated approach with an approach proposed by Groos (2013) with a nearly constant quality factor of 15. The data misfit after the first iteration can be improved by 3.1% with a frequency dependent quality factor.

I want to emphasize that I don't suppose the complete subsurface to be described by one quality factor. Xia et al. (2012) suggest, for example, the estimation of a depth dependent quality factor for each, P-waves and S-waves seperately. Nevertheless, implementing a frequency dependent quality factor leads to a better misfit and, ultimately, accounts for frequency dependent amplitude decay, wherever it might originate from.
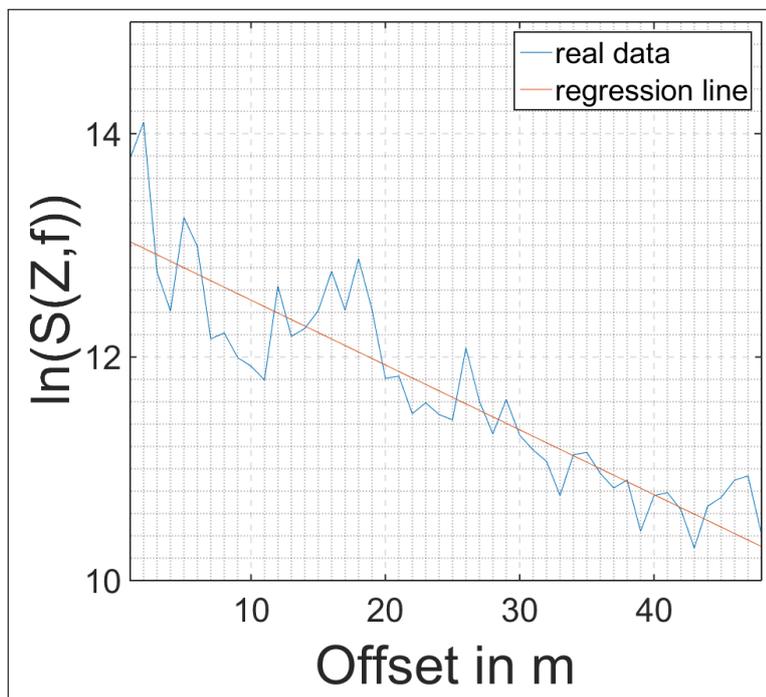
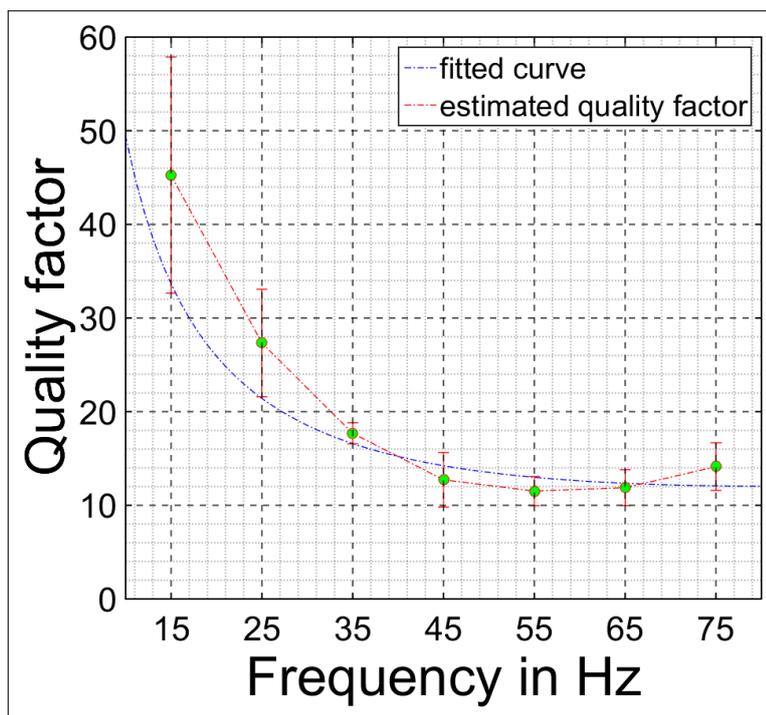Figure 5.2.: Logarithmic plot of the amplitude spectrum with respect to offset.

Figure 5.3.: The plot shows the result of the quality factor estimated from the observed data as well as the fitted values used for the inversion algortihm

5.3. Estimation of Source Signal

If the source signal is unknown one has to simulate a signal, which fits the real source signal in the most appropriate way. First of all we have to reflect what kind of function might be used as a source signal. The hammer impact can be thought of as a force, instantly accelerating the metal plate and subsequently the ground surface. Therefore, the released force might be considered as a Dirac delta function. Nevertheless, the surface exhibits elastic rather than purely rigid characteristics. The presumed force-time function is derived from Forbriger (2004), who analyzes the source signal generated by a hammer blow and estimates half a period of a sine curve as proper fit to the real force. The inversion code simulates half a period of a sine raised to the power 3, to be precise. The time duration of the sine signal is supposed to be chosen accurately in order to serve the source wavelet inversion described in chapter 5.5. In order to estimate the time duration of the real source signal I take a rather rough approach. Both seismic traces 2 meter distant from each source are summed and subsequently divided by their arithmetic mean. Two source locations at each end of the profiles are disregarded, since they don't fulfill the requirement of one trace to each side. The obtained traces for profile one as well as profile two are plotted in figure (5.4) and numbered beginning with the westernmost source. The first arrivals exhibit a cycle period of approximately 0.01 seconds. However, the forward modeling is limited to a ratio of grid points per wavelength of at least 5 suggested by Levander (1988) with the used inversion code (see 3.2). Therefore, I implement a source signal with a half period of 0.011 seconds, which seems sufficient for the inversion of the source wavelet. Besides, the seismic signals are filtered during the inversion process anyway, that a loss of information is unlikely, which would be provided by high frequency content.

5.4. Regularization

DENISE saves the gradient models of the misfit function additionally to the inverted models after each iteration step. Without any preconditioning of the gradient models the subsurface model is preferably updated in the source location's vicinity (see also Groos (2013) and Schäfer (2014)). Therefore, I apply a semi-circular filter to the gradient around each shot location, attenuating the gradient to zero at the center of the filter and decreasing in amplitude with an error function shaped manner to the filter's edge. The radius of the filter is $1.5m$ sufficiently mitigating the artifacts around the sources. In order to prevent a loss of model update information around the sources completely, the gradients of each shot location are filtered individually and merged afterwards. Figure (5.5) displays a section of the gradient model illustrating the effect of the semi-circular filter.

Further artifacts are visible at the receiver locations. To encounter for this issue an additional filter is applied smoothing the gradient matrix via a median filter in horizontal direction with a filter size of 23 grid points corresponding to 2.3 meters. This filter length has to be well estimated and is able to improve the results enormously. An approach of applying any kind of filter to the inverted models instead of the gradient models is disregarded, since the tested model filter smooths the model after each iteration step, even though only negligible model update is performed. In order to emphasize the advantage
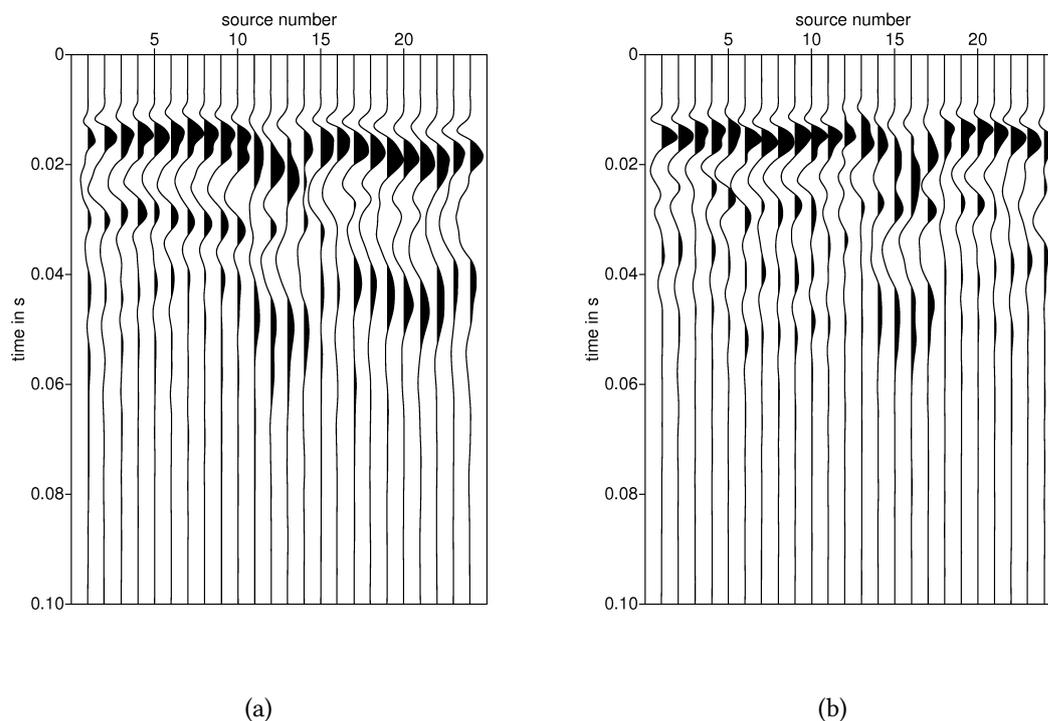
Figure 5.4.: The figure shows the seismic traces 1 meter distant from each of 24 source locations.
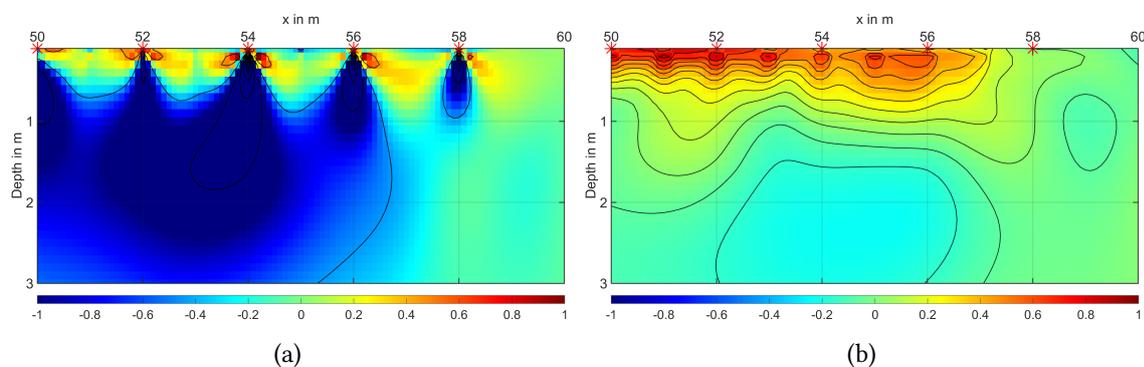

Figure 5.5.: The figure shows a section of the shear-wave gradient model without (a) and with (b) a semi-circular filter applied at the source locations. Red stars mark the locations of the shot positions. The scale is normalized by the maximum amplitude of figure (b) and kept identical in figure (a) in order to emphasize the effect. The remaining high amplitude regions are located at the receiver positions

of a gradient filter in comparison with a model filter one can imagine the situation, where no model update in certain regions is performed due to a good fit of the synthetic and observed data. Then the gradient filter smooths the gradient model with no effect in

such areas, whereas the model filter would smooth the whole model space, no matter if heterogeneities are yet well defined by the data misfit. Nevertheless, it has to be mentioned that a gradient filter increases the total number of iterations.

5.5. Inversion of Source Wavelet

In section 5.3 I described the approach of estimating an appropriate source time function, which resembles the real source signal. However, the synthetic source signal can be fitted more accurately by the use of a source wavelet correction filter (Pratt, 1999). If we assume l unknown Fourier coefficients $\tilde{c}_l$ and the Fourier expansion coefficients of the synthetic data $\tilde{g}_l$ as well as the Fourier expansion coefficients of the observed data $\tilde{d}_l$. The objective is to find complex values for $\tilde{c}_l$ such that the sum of the squared residuals

$$\frac{1}{2}|\tilde{d}_l - \tilde{c}_l \tilde{g}_l|^2 \tag{5.2}$$

is minimized. This yields

$$\tilde{c}_l = \frac{\tilde{g}_l^* \tilde{d}_l}{|\tilde{g}_l|^2} \tag{5.3}$$

Groos (2013) assume several geophone positions and implement a scaling factor f_k for the coefficients with respect to the offset r_k of the *k-th* geophone:

$$f_k = (r_k)^\kappa \tag{5.4}$$

In order to estimate the Fourier coefficients of the source wavelet inversion filter I disregard the traces in direct vicinity of the source, usually closer than 1.5 meters. This is due to overdriven behavior of the geophones. Furthermore, I disregard traces too far from the source, since the source inversion would account for waveforms resulting from the subsurface structure. Usually I account for 6 traces in total at each shot location. It is suggested to estimate an appropriate center frequency of the initially modeled source signal. Otherwise the source time function inversion fails.

6. Results

In this chapter I provide the final results of the applied full waveform inversion, including the inverted source time functions, the fitted seismograms and, finally, the derived subsurface models of profile one and profile two. Furthermore, I present the misfit progress with rising iteration step, which is an important factor for the estimation of the data quality. The subsurface models of both profiles are supposed to reveal similar medium properties but shifted horizontally to each other. Hence, the results of the profiles are compared to proof their validity. I point out, once more, that the focus of this thesis lies on examining the true S-wave velocity model and that the adjustable parameters of the inversion are optimized in this sense. Especially the updated density model, which shows highly inaccurate values, is not taken into account for the choice of an adjusted inversion algorithm leading to more reasonable outcomes. However, the density model does not influence the shape of the forward modeled wave field (see also Schäfer (2014)) and is, therefore, considered negligible. The dimensions of the model spaces are originally 64 meters in horizontal direction and 16 meters in vertical direction, but are truncated in vertical direction to 11 meters depth for the visualization of the results. At the very end of this chapter I give a brief summary of the used computation power and the time consumption of the applied inversion.

6.1. Profile 1

The inversion of the data obtained from the first profile runs more than 90 iterations and is canceled manually, as the data misfit rises noticeable. At iteration step 47 the inversion switches the frequency filter from 30 Hz to 35 Hz due to the achievement of the abort criterion, resulting in very small-scale model parameter updates, which do presumably not reflect the real subsurface properties any more. Therefore, the provided results arise from iteration step 46 corresponding to an inversion of seismic traces, which are filtered with a 30 Hz second order Butterworth filter.

Inverted Source Time Function

Figure 6.1 shows the inverted source signals at each shot location, as they are utilized for the 46th iteration step. The synthetic source signals resemble the real source time functions accurately (compare figure 6.1). However, a second wave peak arises at approximately 0.1 seconds, presumably evoked by overdriven geophones close to the source. As mentioned before, traces can be disregarded for the inversion of the source time function, but the impact of involving too many distant receivers leads to source signals involving the response of the subsurface. This effect can be demonstrated at shot number 28 and gently

at shot number 27, which exhibit a wavelet corresponding to the viscoelastic behavior of the medium. Hence, the consideration whether to omit traces in the source wavelet inversion or not is a balancing act. The similar shape of the inverted source signals is an indicator for the reliability of this process. The modeled sources in the area of the Ettlinger Linie can not be distinguished from other source locations, whereas the real signals close to the sources (compare figure 5.4(a)) exhibit varying frequency content. That effect can be explained by the advanced model update. The Low velocity zone is already well defined and the source wavelet inversion, performed at each frequency shift, accounts for the updated subsurface properties.
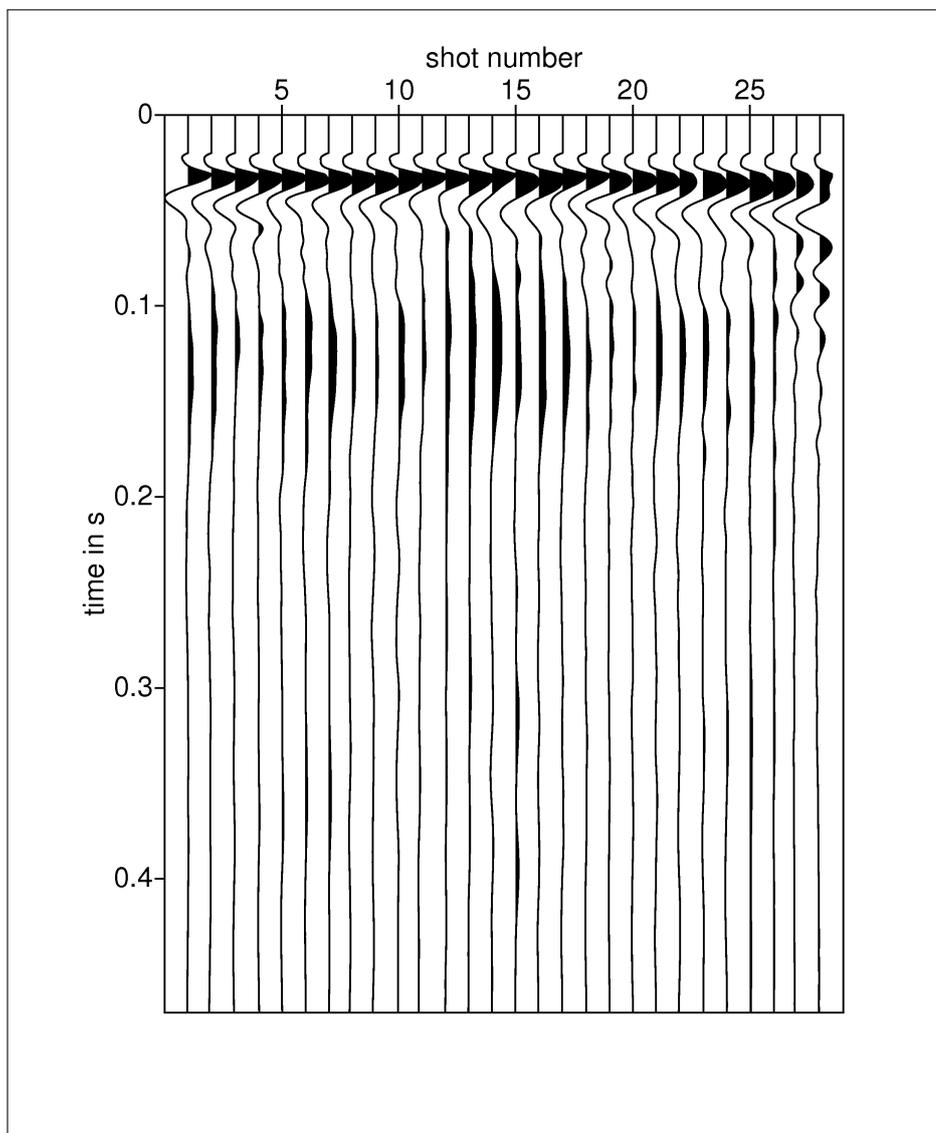
Figure 6.1.: Inverted source time functions of each source at profile 1. The shot numbers correspond to source locations in the field beginning from west to east.

Fitted Seismograms

The recordings of the observed and computed seismic wave fields after 46 iterations are displayed in figure (6.2). The wave fields exhibit, predominatly, a very good fit of each trace from near to far offset, except from the synthetic signals recorded at the receivers adjacent to the source location. The final synthetic seismograms show some kind of fluctuation in the vicinity of the source location especially at shot number 8, whereas the initial synthetic seismograms have a smooth curve singnature. Furthermore, high frequency content is not visible in the inverted source signals (figure 6.1), concluding that it is impossible to receive such signals. If we have a closer look at the inverted source time functions we can observe a steep inset of the very beginning of the wavelet. It is assumed that the high frequency content of the simulated wave field might be caused by this abrupt inset and a resulting effect of grid dispersion. Nevertheless, this effect is assumed to influence the model update quality barely, as it occurs only at few receiver locations and, even more important, should not be accounted for until switching to very high frequencies in the inversion process.
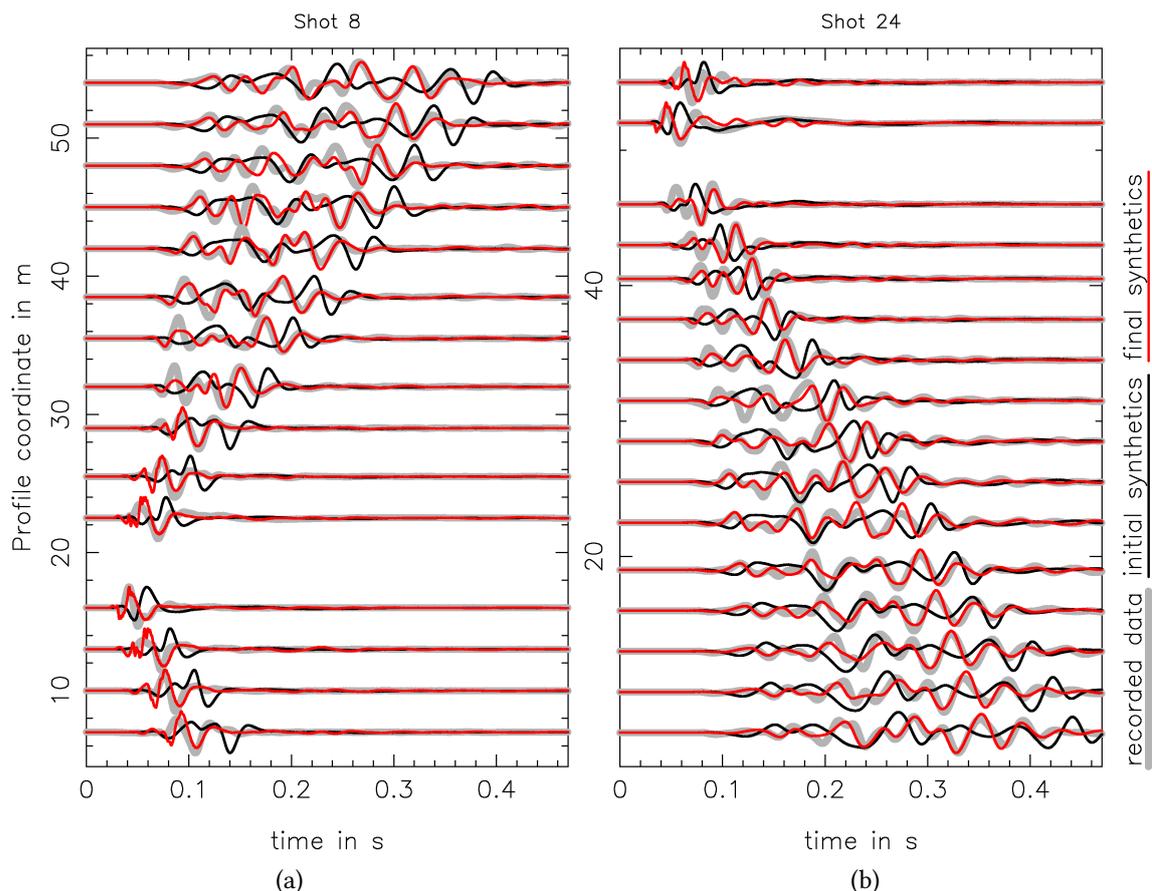
Figure 6.2.: Shot gather of two different shot locations. The grey curve represents the recorded data, black is the initial forward modeled data curve and the red line the fitted synthetic signal after 46 iterations

The inversion is applied incrementally to signals with low frequency content (5 Hz) to higher frequency content (30 Hz) with steps of 5 Hz. It is worth mentioning that most of the model update is performed on the basis of data filtered with a 5 Hz low pass filter, as can be seen in figure (6.3). It takes 23 iterations before switching from 5 Hz to 10 Hz (see table 6.1). At the same time I want to point out to the remaining frequency content after applying the filter (figure 4.2), where even signals with a frequency content of 30 Hz are still dominant.
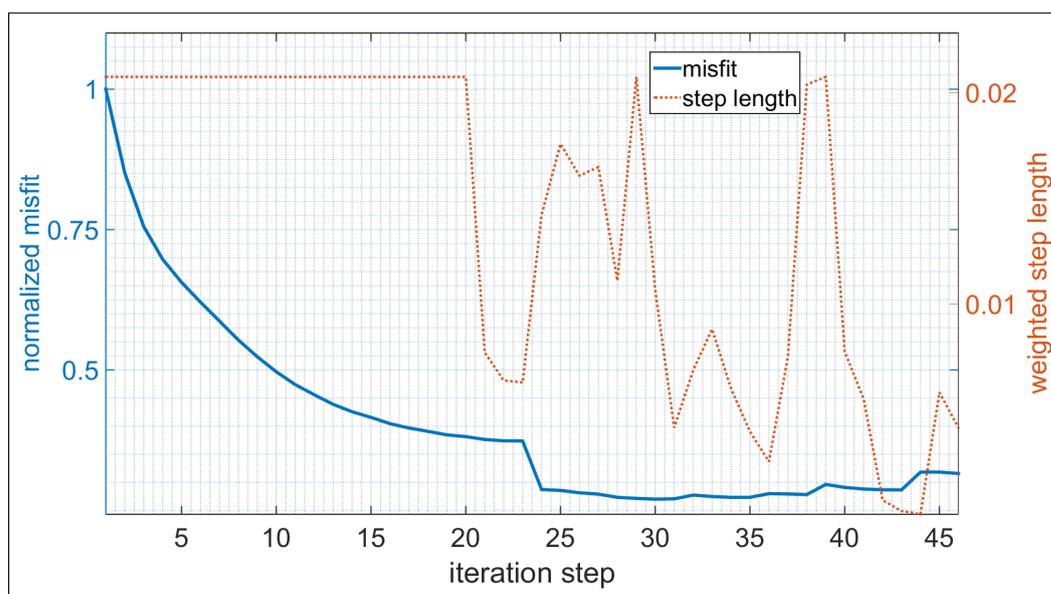
Figure 6.3.: Misfit progress during the inversion of profile one. The blue line denotes the misfit of each iteration step normalized by its maximum. The doted brownish line defines the applied step length for each iteration step in percent as described in section 3.4.3

filter frequency	5 Hz	10 Hz	15 Hz	20 Hz	25 Hz	30 Hz
iteration step	1 to 23	24 to 31	32 to 35	36 to 38	39 to 43	43 to 46

Table 6.1.: Iteration steps with the corresponding filter frequencies obtained from the inversion of profile one

Final Subsurface Models

The results of the inverted subsurface models are plotted in figures 6.4 to figure 6.6 containing the model parameter S-wave velocity, P-wave velocity and mass density. First of all I focus on the shear wave velocity model, which contains the predominant energy content of the measured surface waves. A low velocity zone is projected in the center of the investigation site at 32 meters with a depth of a little over 2 meters and a width at the topmost surface of approximately 8 meters and dropping to 6.5 meters width in 2 meters

depth. The shape of the low velocity zone matches the specifications of the "Ettlinger Linie" compared to historical descriptions (Lang, 1907) and to previous studies (e.g. (Stövhase, 2015), (Lüttschwager, 2014)). At approximately 40 meters the seismic velocities decrease in the topmost layer to 100 $\frac{m}{s}$, which can probably referred to the vicinity of the woodland and a thicker layer of soil than distant from the forest (see figure (2.2). In the west of the Ettlinger Linie, that is at x-coordinates with values below 26 meters, heterogeneities emerge by means of alternating areas of low and high velocities. These heterogeneities are presumably caused due to the choice of an inappropriate initial model. However, the real subsurface exhibits slightly increasing S-wave velocities from west to east (left to right), hence it is not possible to resemble the real subsurface with an one-dimensional synthetic model. Why I don't choose to modify the initial model and use a two-dimensional model instead, is for two reasons. The first depends on the comparability of the results from profile one and profile 2. And the second is to show that the inversion algorithm is capable of reconstructing the subsurface structure with an primitive starting model, as will be demonstrated in the section of the results for profile 2.
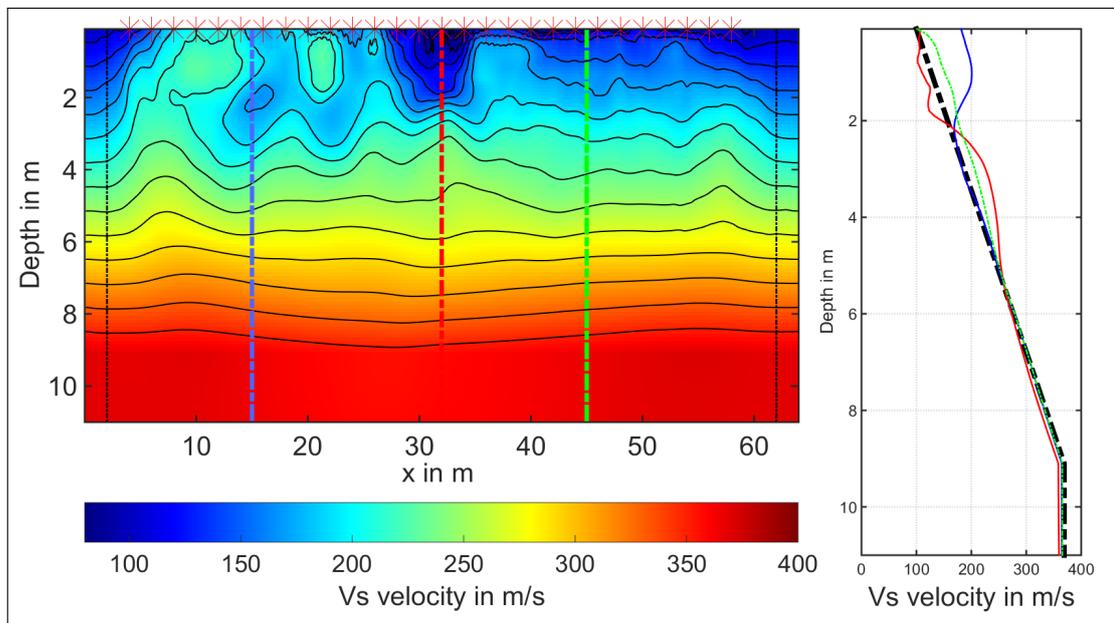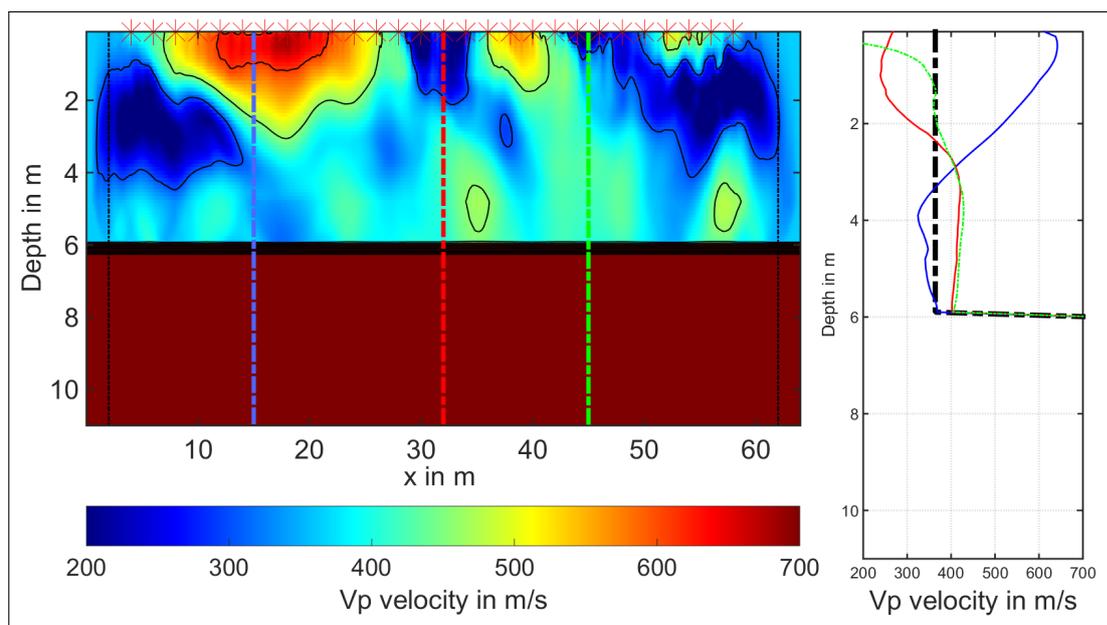

Figure 6.4.: Final model of the S-wave velocities and corresponding cross sections at selected positions (15 m, 32 m, 45 m). At the edges of the image are perfectly matched layers (PML) marked by a black dashed line, where the forward modeled wavefield is damped to zero. No model update is supposed to happen in this regions.

The final P-wave velocity model (figure 6.5) shows extremely local variations with alternating regions of low and high velocities. Their evolution arises at the very beginning of the inversion algorithm, where a high velocity zone at the center of the model is formed and shifts apart to the edges of the model space as the iterations proceed. The remnants can still be located at x-coordinate 18 meters and a small region at 54 meters at the topmost of the model. The surrounding low velocity zones evolve as a result of the high velocity

regions as if to compensate for too high velocities. The occurrence of this phenomenon might result from a misinterpretation of the dispersed wave field of the Rayleigh wave as the direct wave and additionally shifting the phase with offset. That is a quite vague interpretation, but a more reasonable explanation can not be extracted from the obtained synthetic recordings. However, the low velocity zone in the region of the expected Ettlinger Linie arises in later iteration steps and seems to be only marginally influenced by the heterogeneities. The depth correlates with the one achieved for the S-wave velocity model, whereas the width is noticeably reduced.

Figure 6.5.: Final model of the P-wave velocities and corresponding cross sections at selected positions (15 m, 32 m, 45 m). At the edges of the image are perfectly matched layers (PML) marked by a black dashed line, where the forward modeled wavefield is damped to zero. No model update is supposed to happen in this regions. The scale is cut to 700 meters per second, since only negligible model update is performed in a depth beyond 6 meters. The half space consists of seismic velocities of approximately 1836 meters per second, just as the initial model.

The inversion of the density has turned out to be a very complex topic. Every slight adjustment of the quality factor and the source signals leads to massive variation of the updated density model. I will not go into detail of the obtained density model but want to mention the extremely high values around the Ettlinger Linie.
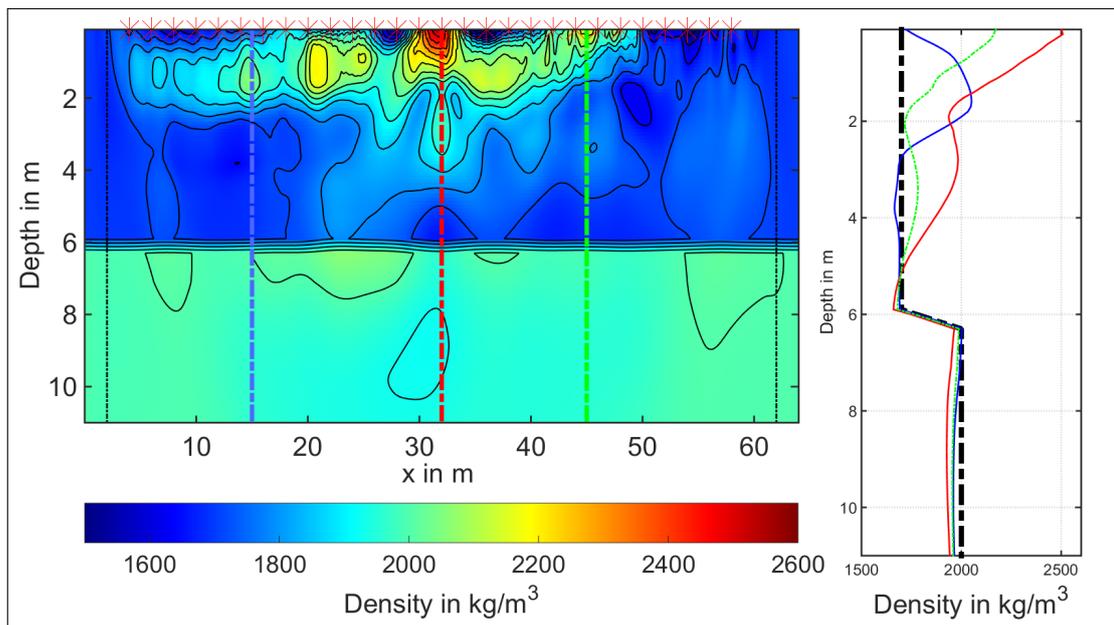
Figure 6.6.: Final model of the mass density and corresponding cross sections at selected positions (15 m, 32 m, 45 m). At the edges of the image are the perfectly matched layers (PML) marked (black dashed lines), where the forward modeled wavefield is damped to zero. No model update is supposed to happen in this areas. The peak value of the density directly at the surface of the Ettlinger Linie exceeds 2500 kg per m^3.

6.2. Profile 2

As for profile one, the inversion algorithm is canceled manually after 90 iterations, where the data is filtered with a low pass filer of 90 Hz. Already at iteration step 47, however, when the filter frequency changes to 35 Hz (see 6.2), the updated model parameters get very local to be reasonable any more. Hence, the results of profile two correspond to iteration step 46 and a filter frequency of 30 Hz, that is exactly as for profile one and is completely by coincident.

Inverted Source Time Function

The inverted source signals of the shot locations for profile two reveal similar progress as the ones estimated at profile one. Again, the natural period of the geophones are visible at almost each trace plotted in figure 6.7 with little higher intensity than in the case of the source time functions for profile one. It is assumed that these wave forms hardly influence the quality of the inversion, since the generated initial synthetic wave fields (see figure 6.8) completely lack this low frequency content. The insets at the very beginning of the seismograms exhibit a very steep progression. As I mention in the previous chapter using the example of profile one, this inset might result in high frequency content of the resulting synthetic seismograms, but is assumed to decrease the data quality barely.
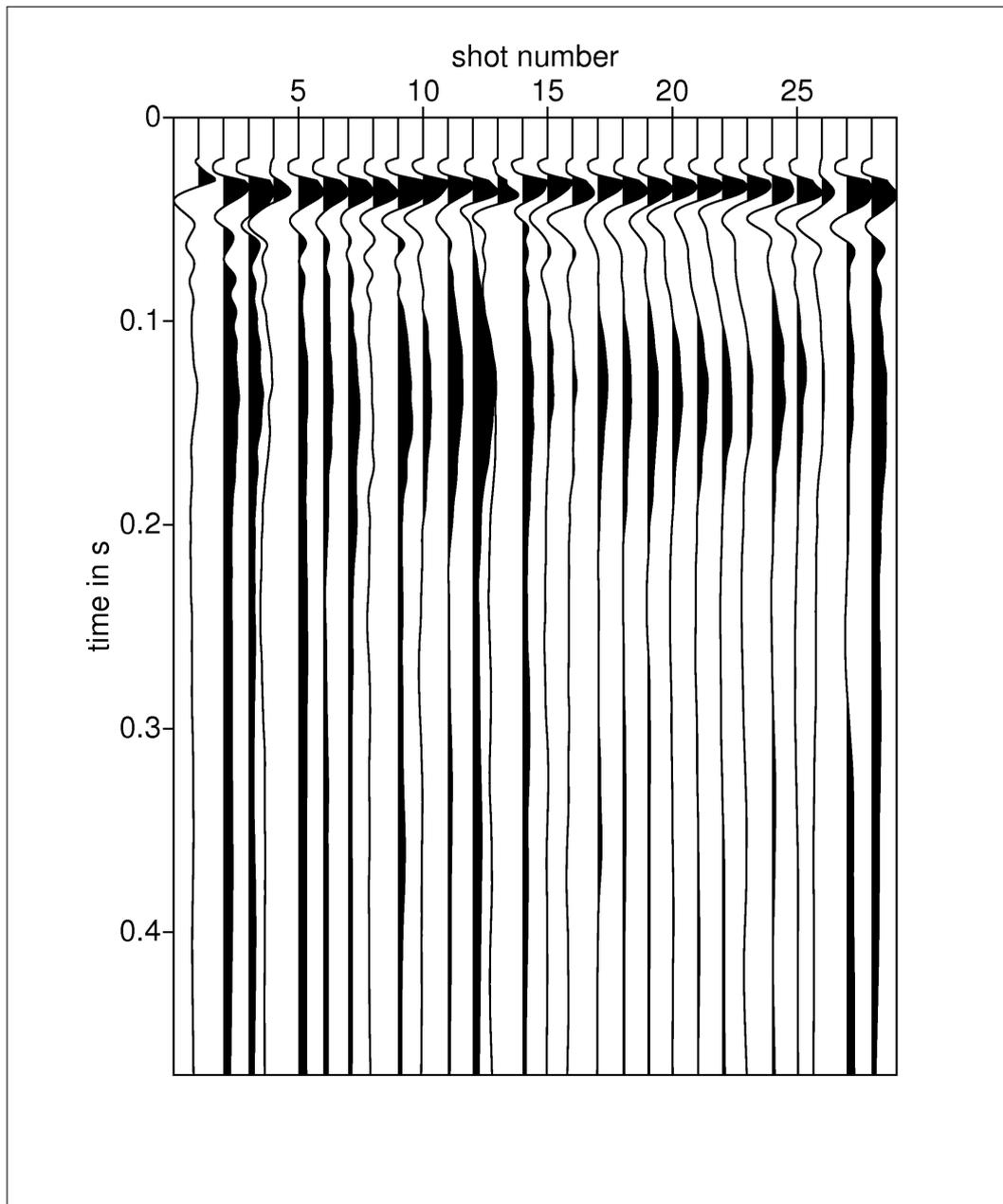
Figure 6.7.: Inverted source time functions of each source at profile 2. The shot numbers correspond to source locations in the field beginning from west to east.

Fitted Seismograms

Figure 6.8 shows the fitted seismograms after 46 iterations for two different shot gathers. The modeled and observed data correlate not as much as in the examples of profile one, but is still a reasonable result in terms of field data application. The synthetic seismograms of shot gather 8 as well as shot gather 24 seem to be slightly out of phase compared to the observed data, nevertheless, the shape of the signals are quite similar. The first two traces to each side of the source of shot gather 8 contain high frequency content, as it is observable for profile one. The reason for this manner is possibly the same as described for profile one. The inverted source signals plotted in figure (6.7) are smooth and do not exhibit high frequency content at all, but exhibit a steep inset at the beginning. Again, it is assumed that this abrupt emergence might cause the high frequency content. The fitted seismograms for shot number 16 are additionally displayed in figure A.2.
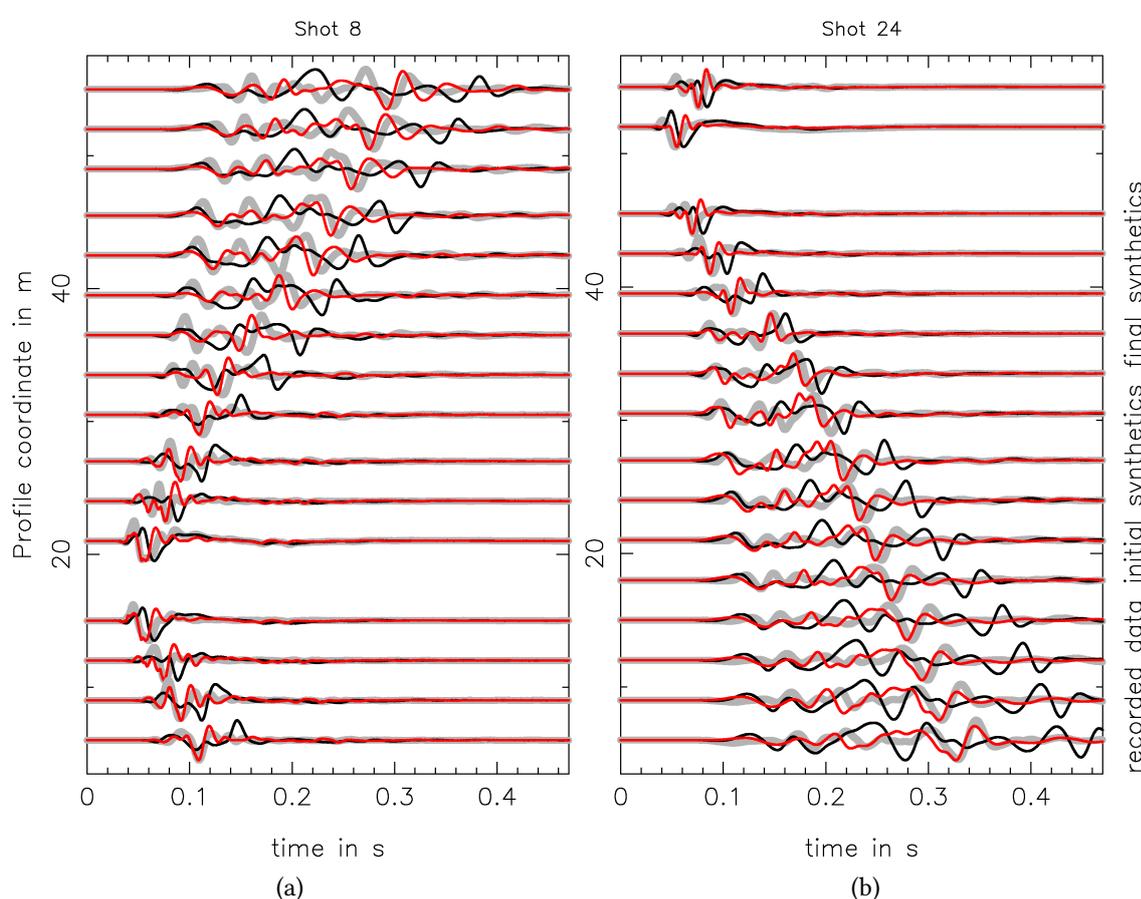
Figure 6.8.: Shot gather of two different shot locations. The grey curve represents the recorded data, black is the initial forward modeled data curve and the red line the fitted synthetic signal after 46 iterations

If we have a look at figure 6.9, it is obvious that misfit reduction is largely achieved during the first 28 iterations with a step length of the adjusted maximum. At iteration step

28 the applied frequency filter switches from 5 Hz to 10 Hz, but again, I want to refer to the remaining frequency content displayed in figure 4.2.
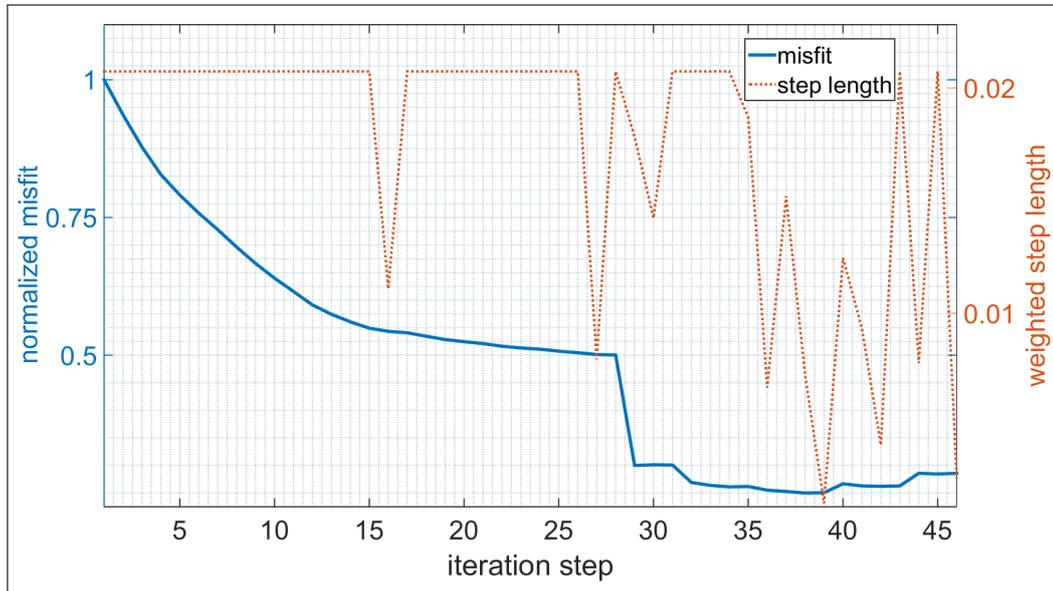

Figure 6.9.: Misfit progress during the inversion of profile two. The blue line denotes the misfit of each iteration step normalized by its maximum. The doted brownish line defines the applied step length for each iteration step in percent as described in section 3.4.3

filter frequency	5 Hz	10 Hz	15 Hz	20 Hz	25 Hz	30 Hz
iteration step	1 to 28	29 to 31	32 to 35	36 to 39	40 to 43	44 to 46

Table 6.2.: Iteration steps with the corresponding filter frequencies obtained from the inversion of profile 2

Final Subsurface Models

The final subsurface models of the parameter spaces S-wave velocity (figure 6.10), P-wave velocity (figure 6.11) and mass density (figure 6.12) of the second profile are presented in this section. I start off with description of the inverted S-wave velocity model, which shows comparable values to profile 1. A low velocity zone at approximately 38 meters is reconstructed with similar dimensions, but shifted along the x-axis. Remember that profile 2 is aligned parallel to profile 1, but does not cross the Ettlinger Linie in its center. Besides, reveals the final model a zone with decreasing velocity values beginning from 48 meters such as the velocity model of profile 2 does. The subsurface model exhibits, furthermore, almost negligible lateral medium properties between 10 and 30 meters, what we would expect in this section of the investigation site. A drawback is the drop shaped formation at the left part of the model, presumably resulting from synthetic source signals, which already contain information about the subsurface in the form of the propagating

wave field. In order to prevent such a lack of model update one has to make sure not to utilize distant seismic traces for the inversion of the source time function. A closer look has to be taken at the region between Ettlinger Linie and the drop of velocity at around 48 meters. It might be interpreted as artifact caused for example by corrupted source signals, however, the same structure can be observed in profile 1 with nearly the same extent. An explanation could be given by examining the structure of the trench, which is still existent in the forest close to the study area. In fact, the material of the trench was deposited directly next to it, exactly where the higher velocities appear in the model. It might have come to compaction of the underlying material and subsequently to increasing seismic velocities. Just as for profile 1 does the penetration depth of the model update roughly exceed 4 meters.
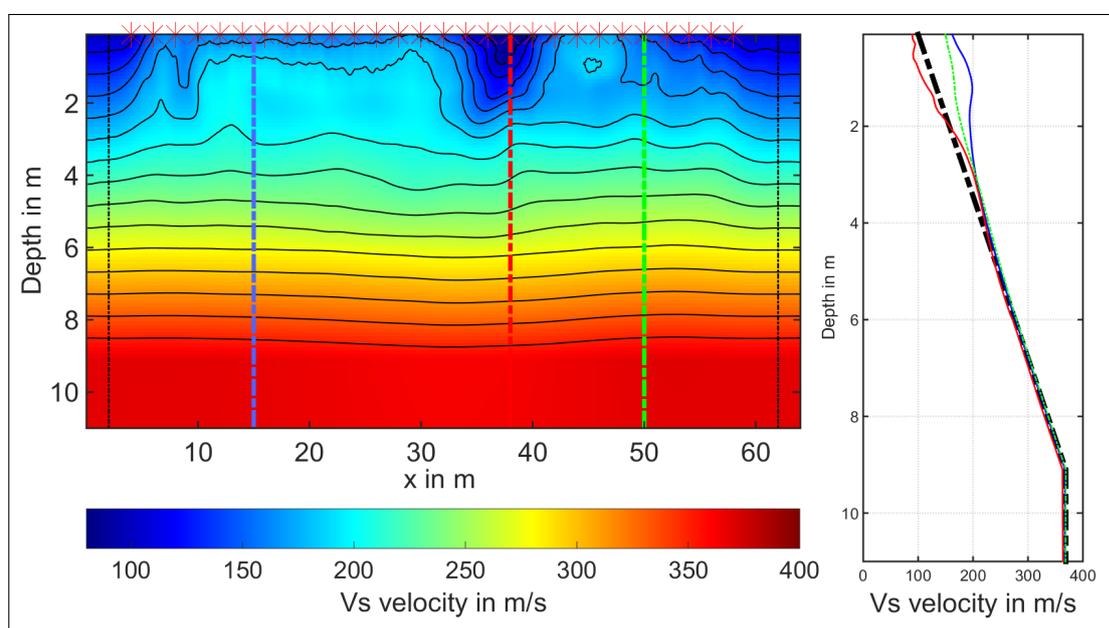
Figure 6.10.: Final S-wave velocity model and corresponding cross sections at selected positions (15 m, 38 m, 50 m). At the edges of the image are perfectly matched layers (PML) marked by a black dashed line, where the forward modeled wavefield is damped to zero. No model update is supposed to happen in this regions.

The final model of the P-wave velocity of profile two (figure 6.11) reveals similar heterogeneities as the result of the velocity model of profile one does, with an even higher degree. The development of this zones progress exactly in the same way as described for profile one. A possible explanation might be that the inversion algorithm accounts for refracted waves as direct waves, which would definitely lead to higher velocities. Nevertheless, the focus of this thesis is to determine an appropriate S-wave velocity model and a further examination would be beyond the scope of this work. It is yet worth mentioning that a low velocity zone evolves in the area of the expected location of the Ettlinger Linie.
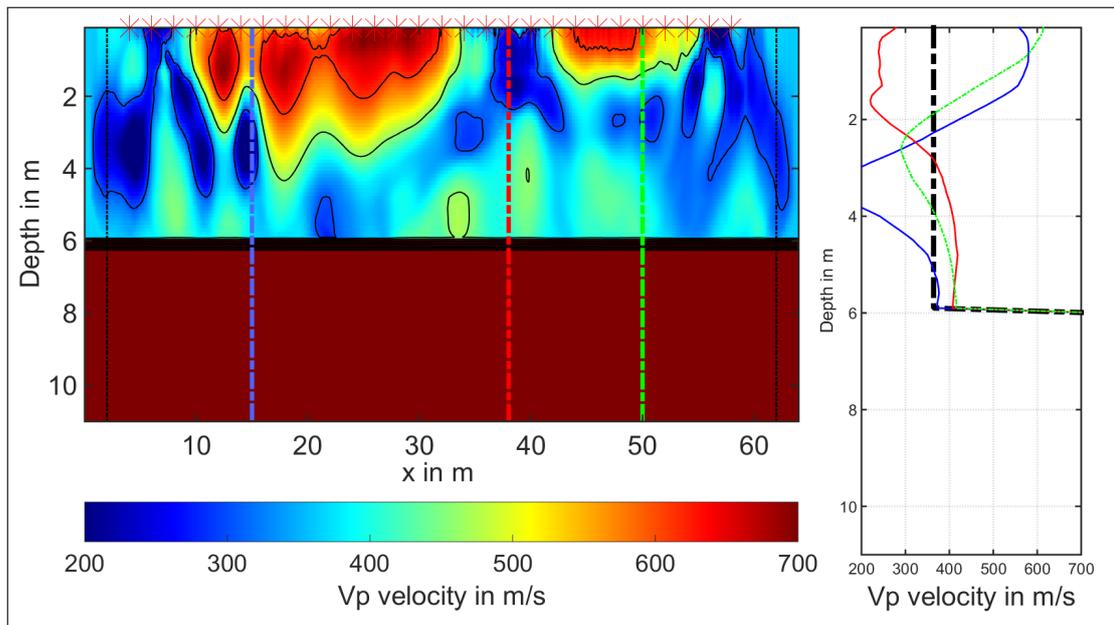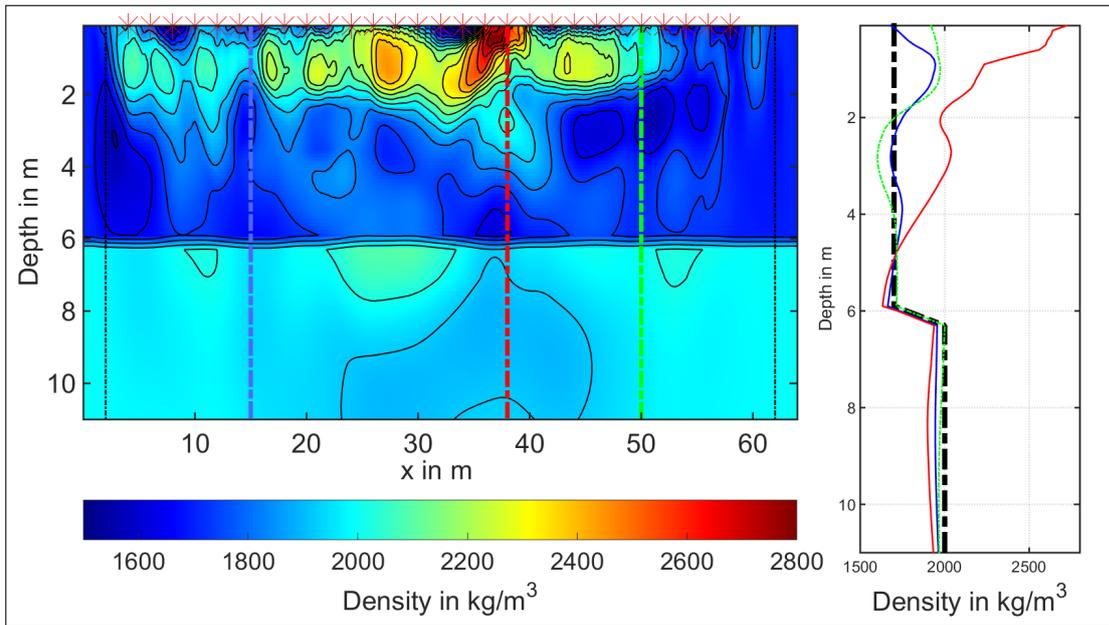
Figure 6.11.: Final P-wave velocity model of profile two and corresponding cross sections at selected positions (15 m, 38 m, 50 m). At the edges of the image are perfectly matched layers (PML) marked by a black dashed line, where the forward modeled wavefield is damped to zero. No model update is supposed to happen in this regions.

The result of the density model for profile two is quite similar to profile one. Again, we can locate a very high density value at the position of the expected low velocity zone. Further singularities are distributed all over the model space, but tend to emerge in the vicinity of the source locations. I omit additional explanations of the obtained density model, since the inversion for density seems too complex and is, furthermore, not the main focus of this thesis.

Figure 6.12.: Final density model of profile two and corresponding cross sections at selected positions (15 m, 38 m, 50 m). At the edges of the image are perfectly matched layers (PML) marked by a black dashed line, where the forward modeled wavefield is damped to zero. No model update is supposed to happen in this regions.

Computation time

For the performance of the field data inversion I use 64 cores addressed at the high-performance computer InstitutsCluster II (IC2). The waveform inversion of both profiles are performed in a similar way in the sense of grid spacing of the SSG and time sampling of the forward modeled wave fields. Therefore, the following specifications belong to each inversion algorithm.

The model space applied in the inversion process consists of 640 grid points in horizontal direction and 160 grid points in vertical direction in terms of the distribution of the SSG. The grid spacing is chosen to be 0.1 meter, which results in a model space in meters of 64 in horizontal and 16 meters in vertical direction. In order to guarantee a stable forward modeling of the wave fields, the time sampling is 25 μs, btw. 40 kHz. With a total recording time of 0.47 s and 18800 time samples.

The overall computation time of profile one until the 46th iteration step is 481.1 minutes, whereas the computation of the results for profile two takes 497.2 minutes.

It is not possible to speed up the waveform inversion performance by reducing the temporal sampling rate, since the system gets unstable then. The estimation of the step length is performed for every third source location, instead of each source location, which can save a bit time. The choice of a weaker gradient filter may also reduce computation time due to a faster convergence of the misfit.

7. Conclusion

The objective of this thesis is the application of full waveform inversion to Rayleigh waves. Since the main energy propagating along the boundary of a free surface and a solid is stored in the vertical shear wave component of the Rayleigh wave, the estimation of an optimum S-wave velocity model is the main objective.

First of all, the choice of an initial model resembling the true subsurface is a crucial step in order to prevent cycle skipping and, therefore, to get stuck in a local minimum or even provoke the forward model to get unstable, due to extremely high updated model parameters. The degree of the gradient for the shear-wave velocity model determines predominantly the dispersion manner of the propagating surface waves and must be adjusted sensitively. Fortunately, the results obtained by Groos (2013) seem to satisfy the requirements of an initial model. However, it is worth mentioning that I omit to implement the structure of the Ettlinger Linie in the initial model completely, in order to proof the abilities of the FWI code and the result of the shear wave velocity model for each profile seem reasonable. Especially the subsurface model of profile two is assumed to be imaged accurately, compared to previous studies ((Lüttschwager, 2014), (Stövhase, 2015)). The Ettlinger Linie exhibits the dimensions and the location as expected. Hence, it is assumed to be proven that full waveform inversion is capable of reconstructing high lateral property variations of the very shallow subsurface precisely. It is surprising that the penetration depth of the model update does hardly rise beyond 5 meters, if we consider the presence of wavelengths exceeding 10 meters, if not 20 meters. The low penetration depth can result either from a very appropriate initial model or from a lower penetration depth of Rayleigh waves than I expected. Schäfer (2014) observes similar issues and implements the approximate Hessian with an additional depth dependent amplification of the gradients. Nevertheless, this approach leads to slightly better model updates in greater depths, but is omitted due to an immense computation effort of the approximate Hessian.

It has turned out that the quality of the updated model depends extremely on the choice of the source time function, which is utilized in the inversion algorithm. The estimated source time functions, however, do not fully satisfy the expectations of how the real source signal is supposed to look like. On the one hand, we get first impulses with very steep slopes, which is not likely to happen when a hammer is accelerated onto an visco-elastic reacting surface, and on the other hand, the synthetic source signals exhibit oscillations with a duration too long to correspond to the real source signal. I assume that the abrupt insets come from a delay in the trigger mechanism of the hammer blow, resulting in a premature first arrival of the recorded wave field, such that the source time inversion omits the very first part of the recorded signal. However, this phenomenon influences the resulting subsurface models barely, it is visible on the synthetic seismograms, though. Very disturbing is the appearance of the oscillations, which are assumed to correspond to

the dispersive wave field of the Rayleigh wave and contain mandatory information about the depth-dependent velocity progress of the real subsurface model. Therefore, I suggest to involve a rather small number of seismic traces close to the source for the inversion of the source time function, even though one risks to invert for the overdriven receivers in the vicinity of the source locations, which is not unlikely to happen with the used acquisition geometry.

The final subsurface models containing the information about the density as well as the P-wave velocity structure are not applicable for the estimation of the real subsurface, I have to admit. It might be worth trying to invert for those subsurface properties by adjusting the inversion parameter with respect to step length and quality factor. A reduced step length could possibly lead to more prudent model updates and, therefore, prevent extreme values of both material properties. Furthermore, the used quality factor is indeed estimated as a function of frequency, but is assumed constant with respect to the model space. Especially for the inversion of the density appears the estimation of a space-dependent quality factor useful. I conclude that from the emergence of extremely high density values directly beneath the surface of the Ettlinger Linie, where different values for the quality factor are expected. An additional implementation of the inversion for the quality factor might be a reasonable solution, if the density model is supposed to be reconstructed.

Last but not least, the application of FWI to Rayleigh waves in order to characterize the very shallow subsurface is a promising tool, especially for the estimation of the shear wave velocities. This method shows the potential to describe the subsurface properties in detail, even though severe lateral property variations are present.

List of Tables

List of Figures

Bibliography

Aki, K. and P. G. Richards (2002). *Quantitative Seismology*. 2nd ed. University Science Books.

Blanch, J. O., J. O. A. Robertsson, and W. W. Symes (1995). "Modeling of a constant Q: Methodology and algorithm for an efficient and optimally inexpensive viscoelastic technique". In: *geophysics* 60.1, pp. 176–184. DOI: `10.1007/BF01772605`.

Bohlen, T. (1998). "Viskoelastische FD-Modellierung seismischer Wellen zur Interpretation gemessener Seismogramme". PhD thesis. Christian-Albrechts-Universitat zu Kiel.

– (2002). "Parallel 3-D viscoelastic finite difference seismic modelling". In: *Geophysics* 28.8, pp. 887–899. DOI: `10.1016/S0098-3004(02)00006-7`.

Bohlen, T. and E. H. Saenger (2006). "Accuracy of heterogeneous staggered-grid finite-difference modeling of Rayleigh waves". In: *Geophysics* 71.4, T109–T115. DOI: `10.1190/1.2213051`.

Bunks, C. et al. (1995). "Multiscale seismic waveform inversion". In: *Geophysics* 60.5, pp. 1457–1473. DOI: `10.1190/1.1443880`.

Choi, Y. and T. Alkhalifah (2012). "Application of multi-source waveform inversion to marine streamer data using the global correlation norm". In: *Geophysical Prospecting* 60.4, pp. 748–758. DOI: `10.1111/j.1365-2478.2012.01079.x`.

Christensen, R. M. (1982). *Theory of viscoelasticity. An introduction.* 1st ed.

Courant, R., K. Friedrichs, and H. Lewy (1928). "Über die partiellen Differenzengleichungen der mathematischen Physik". In: *Mathematische Annalen* 100, pp. 32–74.

Day, S. M. and J. B. Minister (1984). "Numerical simulation of attenuated wavefields using a Padé approximant method". In: *Geophysical Journal International* 78.1, pp. 105–118. DOI: `10.1111/j.1365-246X.1984.tb06474.x`.

Forbriger, T. (2003a). "Inversion of shallow-seismic wavefields: I. Wavefield transformation". In: *Geophysical Journal International* 153.3, pp. 719–734. DOI: `10.1046/j.1365-246X.2003.01929.x`.

– (2003b). "Inversion of shallow-seismic wavefields: II. Inferring subsurface properties from wavefield transforms". In: *Geophysical Journal International* 153.3, pp. 735–752. DOI: `10.1046/j.1365-246X.2003.01985.x`.

– (2004). "Dynamics of the Hammer Blow". In: *Symposium in Memoriam of Prof. Gerhard Müller* 1.2004, pp. 93–97.

Forbriger, T., L. Groos, and M. Schäfer (2014). "Line-source simulation for shallow-seismic data. Part 1: theoretical background". In: *Geophysical Journal International* 198, pp. 1387–1404. DOI: `10.1093/gji/ggu199`.

Groos, L. (2013). "2D full waveform inversion of shallow seismic Rayleigh waves". PhD thesis. Karlsruhe Institute of Technology (KIT).

Hüttner, R., H. .-.-J. Konrad, and A. Zitzmann (1986). "Geologische Übersichtskarte 1:200 000, Blatt CC7110 Mannheim". German. In: *Bundesanstalt für Geowissenschaften und*

Rohstoffe (BGR) in Zusammenarbeit mit den Geologischen Landesämtern der Bundesrepublik Deutschland. Hannover.

Jeng, Y., J.-Y. Tsai, and S.-H. Chen (1999). "An improved method of determining near-surface Q". In: *Geophysics* 64.5, pp. 1608–1617. DOI: 10.1190/1.1444665.

Köhn, D. (2011). "Time Domain 2D Elastic Full Waveform Tomography". PhD thesis. Christian-Albrechts-Universit zu Kiel.

Köhn, D. et al. (2013). "DENISE - User manual". In: *Christian-Albrechts-Universität zu Kiel und Karlsruher Institut für Technologie.*

Lang, K. (1907). *Die Ettlinger Linien und ihre Geschichte.* 1st ed. G. Braunsche Hofbuchdruckerei Karlsruhe.

Levander, A. R. (1988). "Fourth-order finite-difference P-SV seismograms". In: *geophysics* 53.11, pp. 1425–1436.

Lüttschwager, G. (2014). "Simulation und Feldmessung der Abstrahlung seismischer Vibratoren im Nahfeld". MA thesis. Karlsruhe Institute of Technology (KIT).

Moczo, P., J. Kristek, and L. Halada (2004). *The finite-difference method for seismologists.* Comenius University.

Pratt, R. G. (1999). "Seismic waveform inversion in the frequency domain, Part 1: Theory and verification in a physical scale model". In: *GEOPHYSICS* 64.3, pp. 888–901. DOI: 10.1190/1.1444597.

Schäfer, M. (2014). "Application of full-waveform inversion to shallow-seismic Rayleigh waves on 2D structures". PhD thesis. Karlsruher Institut für Technologie (KIT).

Socco, L. V., S. Foti, and D. Boiero (2010). "Surface-wave analysis for building near-surface velocity models — Established approaches and new perspectives". In: *Geophysics* 75.5, 75A83–75A102. DOI: 10.1190/1.3479491.

Stövhase, J. (2015). "Laufzeittomographie von SH-Wellen zur Charakterisierung der Ettlinger Linie bei Rheinstetten". MA thesis. Karlsruhe Institute of Technology (KIT).

Tarantola, A. (1984). "Inversion of seismic reflection data in the acoustic approximation". English. In: *Geophysics* 49.8, pp. 1259–1266.

– (1988). "Theoretical background for the inversion of seismic waveforms including elasticity and attenuation". English. In: *pure and applied geophysics* 128.1-2, pp. 365–399. DOI: 10.1007/BF01772605.

Virieux, J. (1986). "P-SV wave propagation in heterogeneous media: Velocity-stress finite-difference method". English. In: *GEOPHYSICS* 51.4, pp. 889–901. DOI: 10.1190/1.1442147.

Wathelet, M., D. Jongmans, and M. Ohrnberger (2004). "Surface-wave inversion using a direct search algorithm and its application to ambient vibration measurements". English. In: *Near Surface Geophysics* 2.4, pp. 211–221. DOI: 10.3997/1873-0604.2004018.

Xia, J. et al. (2012). "Estimation of near-surface quality factors by constrained inversion of Rayleigh-wave attenuation coefficients". English. In: *Journal of Applied Geophysics* 82, pp. 137–144. DOI: 10.1016/j.jappgeo.2012.03.003.

Zacharias, S. (2010). "Akquisition und Interpretation von Oberflächenwellen für die Wellenforminversion". MA thesis. Karlsruhe Institute of Technology (KIT).

A. Appendix

Applied Software and Hardware

- DENISE (Köhn, 2011)

- MATLAB R2014a (The Math Works, Inc.)

- Seismic Un*x (Colorado School of Mines)

- high-performance computer InstitutsCluster II (ic2) (Steinbuch Centre for Computing KIT)
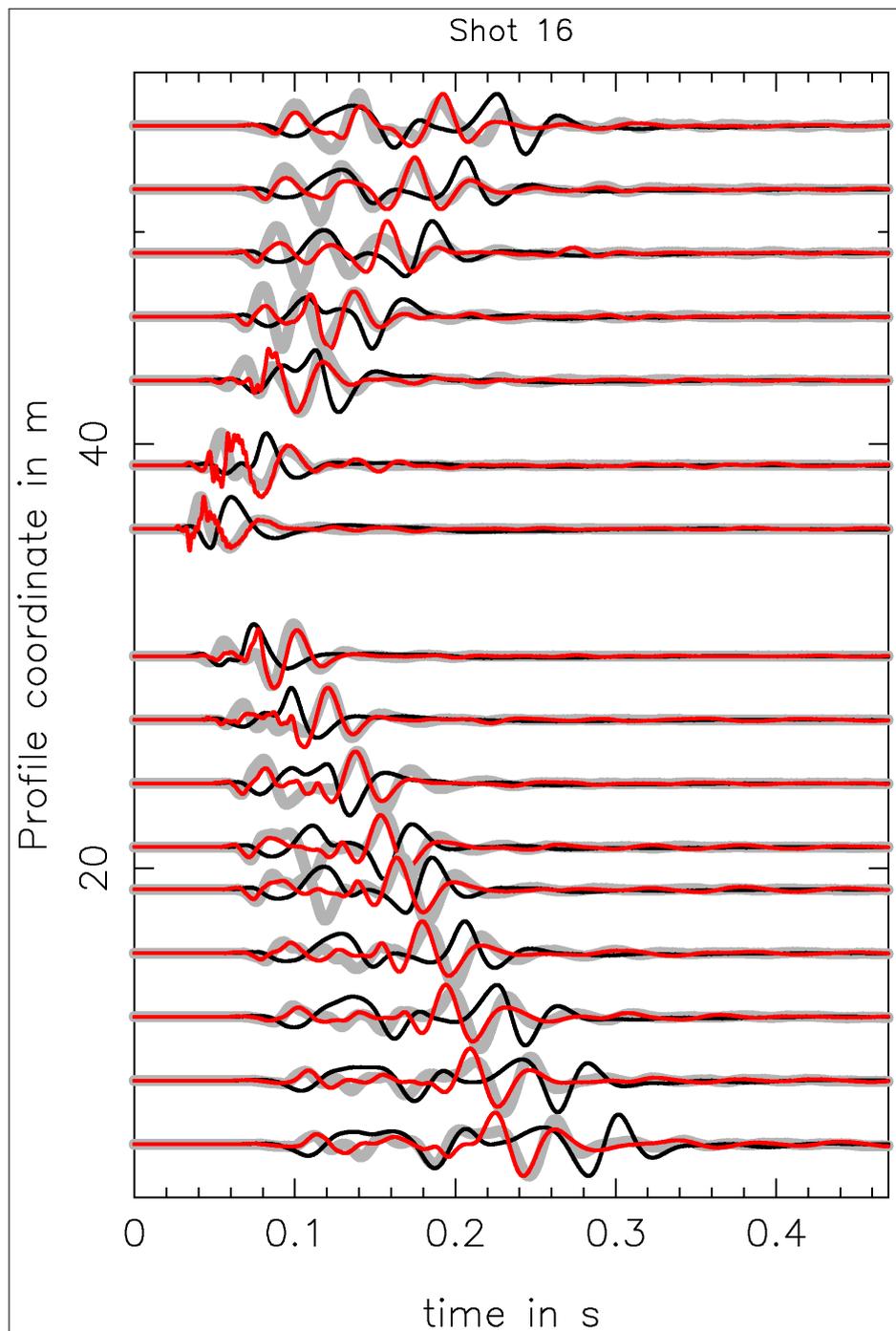
Figure A.1.: Shot gather of the initial model (black), of the inverted final model after 46 iterations (red) and the recorded, real seismograms (grey) of profile one.
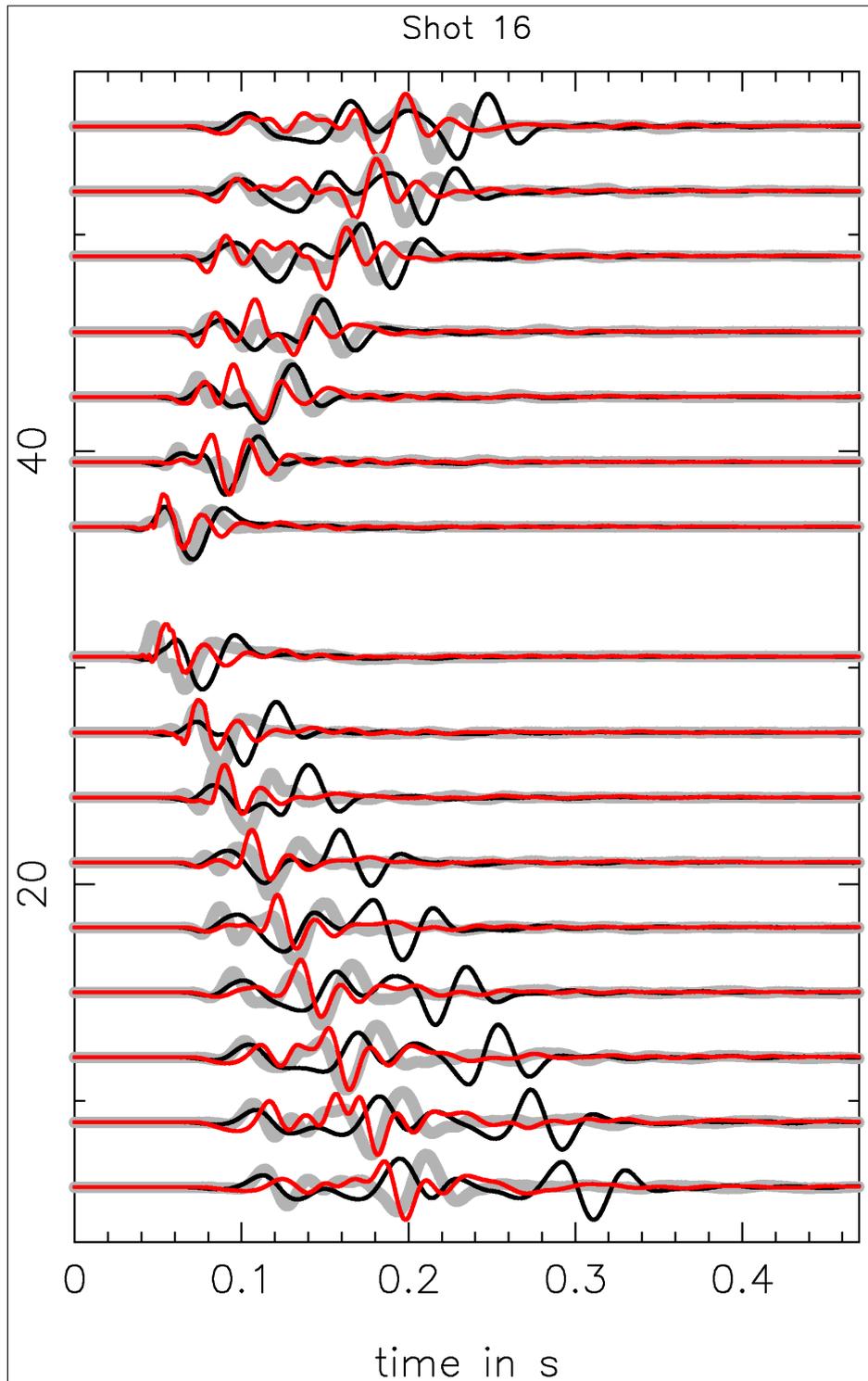
Figure A.2.: Shot gather of the initial model (black), of the inverted final model after 46 iterations (red) and the recorded, real seismograms (grey) of profile two.

Schlusswort

Zunächst einmal möchte ich mich ganz allgemein bei meinen Kommilitonen, Dozenten und Professoren für eine sehr angenehme und interessante Zeit am Karlsruher Institut für Technologie, insbesondere am Geophysikalischen Institut bedanken. Die Atmosphäre war immer freundschaftlich und kollegial und ein Austausch über geophysikalische Problemstellungen wurde immer mit Euphorie geführt. Im Speziellen danke ich zunächst den Doktoranden Niklas Thiel, Tilman Metz und Laura Gaßner, die mir gegenüber viel Geduld aufgebracht haben, ohne sich das anmerken zu lassen. Des Weiteren werde ich anregende Gespräche mit Markus Kunert und Kersten Schlosser vermissen, die sich durch ähnliche Themengebiete schlagen durften.

Mein besonderer Dank gilt meinem betreuenden Professor Thomas Bohlen, ohne dessen Flexibilität eine solch interessante Themenstellung, wie in dieser Masterarbeit bearbeitet wurde, gar nicht erst möglich gewesen wäre.

Für die Feldmessungen wurde mir die Fläche auf dem Segelfluggelände in Rheinstetten bereitwillig überlassen, was in keinster Weise selbstverständlich ist. Der Verantwortliche Herr Michael Hoffmann hat mich in dieser Angelegenheit kooperativ unterstützt.